Scientific Reports

https://doi.org/10.1038/s41598-025-34351-2

Article in Press

Frictional moving load-induced dynamic response of a porous piezoelectric micro/nano plate with superficial parabolic discontinuity

Received: 18 November 2025

Accepted: 28 December 2025

Published online: 03 January 2026

Cite this article as: Meghana A.R., Das S., Dutta R. *et al.* Frictional moving load-induced dynamic response of a porous piezoelectric micro/nano plate with superficial parabolic discontinuity. *Sci Rep* (2025). https://doi.org/10.1038/s41598-025-34351-2

A. R. Meghana, Soumik Das, Rachaita Dutta, Vipin Gupta, Murat Yaylacı, Faisal Muteb K. Almalki, Mohammad Ghatasheh & Aymen Flah

We are providing an unedited version of this manuscript to give early access to its findings. Before final publication, the manuscript will undergo further editing. Please note there may be errors present which affect the content, and all legal disclaimers apply.

If this paper is publishing under a Transparent Peer Review model then Peer Review reports will publish with the final article.

ARTICLE IN PRESS

© The Author(s) 2025. **Open Access** This article is licensed under a Creative Commons Attribution-NonCommercial-NoDerivatives 4.0 International License, which permits any non-commercial use, sharing, distribution and reproduction in any medium or format, as long as you give appropriate credit to the original author(s) and the source, provide a link to the Creative Commons licence, and indicate if you modified the licensed material. You do not have permission under this licence to share adapted material derived from this article or parts of it. The images or other third party material in this article are included in the article's Creative Commons licence, unless indicated otherwise in a credit line to the material. If material is not included in the article's Creative Commons licence and your intended use is not permitted by statutory regulation or exceeds the permitted use, you will need to obtain permission directly from the copyright holder. To view a copy of this licence, visit http://creativecommons.org/licenses/by-nc-nd/4.0/.

ARTICLE IN PRESS

Frictional moving load-induced dynamic response of a porous piezoelectric micro/nano plate with superficial parabolic discontinuity

Meghana A R[1], Soumik Das[1], Rachaita Dutta[2,*], Vipin Gupta[3], Murat Yaylacı[4], Faisal Muteb K. Almalki[5], Mohammad Ghatasheh[6], Aymen Flah[7,8,9]

[1]*School of Physical Sciences, Amrita Vishwa Vidyapeetham, Mysuru Campus, Karnataka, India*

[2]*School of Computing, Amrita Vishwa Vidyapeetham, Mysuru Campus, Karnataka, India*

[3]*Department of Mathematics, Gurugram University, Gurugram, India*

[4]*Department of Civil Engineering, Recep Tayyip Erdogan University, 53100, Rize, Turkey*

[5]*Department of Mathematics, Faculty of Science, Al-Baha University, Alaqiq, 65779-7738, Saudi Arabia*

[6]*Department of Basic Sciences, Middle East University, Amman 11831, Jordan*

[7]*Applied Science Research Center, Applied Science Private University, Amman, 11931, Jordan*

[8]*ENET Centre, CEET, VSB-Technical University of Ostrava, 70800 Ostrava, Czech Republic*

[9]*Centre for Research Impact and Outcome, Chitkara University, Punjab University, Punjab, Rajpura, 140401, India*

[*]*Corresponding author, Email: rachaita.dutta18@gmail.com*

Abstract

The present paper aims to analyze the complex dynamic response of micro/nano-scale components through investigating the stress distribution within a Nonlocal Porous Piezoelectric Layer (NPPEL) of finite thickness. The study specifically focuses on quantifying the combined effects of material porosity, size-dependent elasticity, and geometrical surface imperfections when the layer is subjected to a load moving across its upper boundary. This comprehensive model provides a more realistic assessment of reliability for small-scale smart devices. The layer's constitutive behavior is modeled using Eringen's nonlocal elasticity theory to account for the essential size effects present at the micro/nano scale. The governing equations for the coupled porous and piezoelectric medium are derived, incorporating appropriate boundary conditions for a moving load. Crucially, the superficial parabolic discontinuity on the upper surface is handled analytically through a robust perturbation technique, allowing for the derivation of closed analytical forms for the resulting shear and normal stresses. The final solutions are then computed using Mathematica to illustrate the transient stress fields. Numerical results demonstrate that the nonlocal parameter is highly effective at amplifying the magnitude of the stresses, which is characteristic of the stiffening effect in nonlocal models. The depth and factor of the parabolic irregularity significantly amplify the stress concentrations at the interface, indicating a critical pathway for potential failure. Furthermore, the frictional coefficient of the moving load plays a non-linear role in dictating the shear stress distribution, providing crucial insight into contact mechanics at the nanoscale. The core novelty lies in the simultaneous analytical incorporation of nonlocal effects, porosity, and an arbitrary surface irregularity under dynamic moving load conditions—a combination highly relevant to microfabrication. The model is directly applicable to enhancing the design and performance assessment of MEMS/NEMS pressure sensors, ultra-thin piezoelectric energy harvesters, and other micro-electromechanical devices where surface quality and size effects dictate device lifespan and reliability.

ARTICLE IN PRESS

Keywords

Moving load; Piezoelectric material; Porosity; Nonlocal elasticity; Parabolic irregularity; Perturbation technique

ARTICLE IN PRESS

1. Introduction

Smart materials have emerged as key components across aerospace, civil, mechanical, and biomedical engineering owing to their multifunctional capabilities and adaptability to complex environments [1]. Among these, piezoelectric materials have received significant attention due to their dual functionality as both actuators and sensors, enabling applications ranging from structural health monitoring to precision control systems [2]. Their ability to convert mechanical stimuli into electrical signals and vice versa has motivated extensive research on the behavior of coupled electromechanical structures under various loading conditions [3–5].

Dynamic problems involving moving loads have become increasingly important due to their relevance in transportation engineering, particularly for high-speed trains, highway systems, and mechanized transit [6,7]. Pioneering studies on vehicle–bridge, vehicle–pavement, and train–track interactions have demonstrated the critical influence of moving loads on vibration, stability, and long-term performance of layered structural systems [8–10]. These works collectively highlight that understanding stress development in layered or heterogeneous media under moving excitations remains a major engineering challenge, especially as structural systems become more lightweight and multifunctional. Historical developments in moving-load theory laid the foundation for contemporary analyzes. Sneddon [11] provided one of the earliest formulations for stresses induced by slowly moving loads over an elastic half-space . Subsequent analytical advances by Ang [12], Payton [13], and Sackman [14] extended the framework to transient and finite-domain settings. Further studies incorporated geometric imperfections and irregularities; for example, Chatterjee and Chattopadhyay [15] examined the influence of parabolic surface irregularities on stress fields in floating ice sheets under moving loads. More recent contributions have integrated advanced material systems—such as functionally graded, anisotropic, or porous media—into moving-load models [16–18].

Within this broader context, porous piezoelectric materials have gained prominence as researchers seek to overcome the high density, acoustic impedance, and brittleness of conventional piezoelectric ceramics [19]. Introducing controlled porosity leads to improved electromechanical performance, enhanced acoustic matching, and greater tunability of material behavior [20, 21]. Piezoelectric materials, owing to their electromechanical coupling, generate electric charges under mechanical deformation and conversely deform elastically in electric fields [22]. These materials find wide applications in sensors, actuators, energy harvesters, and smart structures [23]. However, monolithic piezoelectric substrates face challenges such as high density, acoustic impedance mismatch, and brittleness, which porous piezoelectric composites mitigate by reducing density and improving acoustic compatibility [24]. Porosity notably affects parameters like elastic moduli, dielectric constants, and viscosity, tailoring piezoelectric responses for applications including contact microphones and underwater transducers [25, 26]. Sophisticated analyses of porous and visco-porous piezoelectric structures under dynamic loading have demonstrated the significant influence of both porosity distribution and viscoelastic damping on the coupled response.

Recent investigations emphasize the critical role of imperfections and environmental factors on wave propagation and stress distributions in piezoelectric media. Studies by Gupta et al. [27] analyzed circumferential SH waves in graded cylindrical piezoelectric structures with interfacial imperfections. Seema et al. [28] demonstrated that surface elasticity significantly influences acoustic wave velocity and energy transmission in piezoelectric layers. Wave damping effects in layered systems immersed in viscous fluids were explored by Cui et al. [29], while Liu et al. [30] studied pre-stress impacts on Love waves relevant to sensor technology. Furthermore, Kumhar et al. [31] highlighted wave behavior in porous piezo-composites with interfacial discontinuities, important for biosensing, and Moharana [32] proposed continuum shear-lag models detecting structural damage through frequency shifts of SH waves.

Surface irregularities and interface imperfections further complicate stress generation in layered piezoelectric systems. Irregular geometries introduce localized stress concentrations and signif-

ARTICLE IN PRESS

icantly modify acoustic and elastic wave propagation, making their consideration essential for realistic modeling of piezoelectric plates, smart structures, and geophysical media [33, 34]. Such geometrical deviations—whether in the form of surface corrugations, waviness, or micro-scale roughness—are known to cause scattering, attenuation, and mode conversion of guided waves, thereby influencing sensing and actuation efficiency [35, 36]. Moreover, imperfect bonding conditions in layered microstructures strongly affect electromechanical coupling, dynamic stiffness, and stress transfer across interfaces.

The trend toward miniaturization in smart structures necessitates the incorporation of nonlocal elasticity, which accounts for long-range interatomic interactions and size-dependent mechanical behavior. Developed by Eringen and Edelen [37, 38], nonlocal elasticity addresses limitations of classical continuum theory by eliminating stress singularities and more accurately representing nanoscale phenomena. The nonlocal framework has since been widely applied to carbon-nanotube-based structures [39–41], nanoscale vibration problems [42, 43], and functionally graded nanoplates [44]. Nonlocal effects on wave propagation in porous and viscoelastic media have also been investigated in recent works [45–47]. MEMS and NEMS are integrated systems that combine mechanical and electrical components at the micro ($10^{-6}m$) and nano ($10^{-9}m$) scales to function as sensors, actuators, and resonators. They include diverse types such as accelerometers, gyroscopes, and lab-on-a-chip devices, which are essential for modern technology. These systems are widely applied in smartphones for motion sensing, automotive safety for airbag deployment, and healthcare for high-precision medical diagnostics. The study by Liyuan Wang et al. [48] focuses on the nonlinear vibration analysis of nonlocal fractional viscoelastic piezoelectric nanobeams, which also incorporates surface effects. The nonlocal dynamic and resonance responses of multifunctional Functionally Graded Porous micro/nanobeam adsorbers under multi-physics coupling for highly sensitive biosensing applications have also been investigated in recent works [49–51]. The nonlinear thermal effect on a perforated Functionally Graded Porous bio-resonator was studied by Yahia Maiza et al. [52] using the nonlocal strain gradient theory and the Differential Quadrature Method. The studies [53, 54] examines the effect of adsorption, shear distortion, and small-scale effect on the resonant frequency shifts of biomolecular resonators under thermomagnetic conditions. Mektout et al. [55] developed a functional, resonator-based, nonlocal Functionally Graded Porous hollow adsorber to detect coupled biomolecules using the Differential Quadrature Method framework.

Despite a substantial body of research in continuum mechanics, existing studies have examined porous piezoelectric layers, nonlocal elasticity, and moving-load problems largely in isolation. To the best of our knowledge, no published work has investigated the combined effects of nonlocal elasticity, porosity, piezoelectric coupling, frictional loading, and geometric surface irregularity within a unified analytical framework. This represents a significant knowledge gap, given the increasing reliance on porous piezoelectric layers in microscale sensors, actuators, surface acoustic wave devices, and energy harvesters. Furthermore, while most research on nonlocal porous piezoelectric media remains limited to static or basic wave-propagation scenarios, the present work addresses a more challenging and practically relevant dynamic frictional moving-load problem. The present research fills this theoretical void by analytically evaluating the induced stresses and electric potentials in a nonlocal porous piezoelectric layer (NPPEL) featuring a superficial parabolic irregularity. By employing a perturbation-based solution methodology, we derive closed-form expressions for the field components while incorporating appropriate mechanical and electromechanical boundary conditions. The novelty of this study lies in capturing transient electromechanical interactions that have not been previously modeled, specifically revealing how the simultaneous inclusion of long-range nonlocal interactions, pore-fluid contributions, and piezoelectric coupling governs stress transmission. The primary contribution of this work is a qualitatively new understanding of how friction, surface geometry, load velocity, and microstructural scale effects interact at the micro/nano scale. By systematically analyzing critical parameters—including the friction coefficient, irregularity depth, surface factor, and nonlocal scaling parameter—this study advances the

ARTICLE IN PRESS

theoretical understanding of moving-load-induced responses in size-dependent porous structures. Ultimately, this research provides a rigorous foundation for the optimized design and performance prediction of next-generation smart plates and nano-electromechanical systems (NEMS) characterized by surface irregularities.

A detailed clarification of the preceding terms, as well as other terms discussed subsequently, is summarized in the Table 1.

Table 1: List of symbols with definitions

.

Notations	Definition	Notations	Definition
v_i	Displacement component for nonlocal porous piezoelectric layer	Υ^*_{ij}	Fluid pressure
Φ^*	Electric potential function of fluid phase	Φ	Electric potential function of solid phase
Υ^{nl}_{ij}	Nonlocal stress tensor of porous piezoelectric layer	Υ^{l}_{ij}	Local stress tensor
D_i	Electric displacement component of solid phase	D^*_i	Electric displacement component of fluid phase
E_i	Electric field component of solid phase	E^*_i	Electric field component of fluid phase
$\mathcal{C}_{ijkl}, \mathcal{M}_{ij}$	Elastic constants of solid	$\mathcal{A}_{ij}$	Dielectric constant
$\mathcal{E}^*_i$	Piezoelectric moduli of fluid	$\mathcal{E}_{ij}$	Piezoelectric moduli of soild
χ_{ij}, χ^*_i	Piezoelectric coupling between solid and fluid phase	$(\varrho_{11})_{ij}$, $(\varrho_{22})_{ij}$, $(\varrho_{12})_{ij}$	Mass coefficients
ς_{ij}	Dielectric permittivity for solid phase	ς^*_i	Dielectric permittivity for fluid phase
Γ_{ij}	Strain component for solid phase	Γ^*	Dilatation for the fluid

ARTICLE IN PRESS

2. Derivation of fundamental relations for nonlocal fluid-saturated porous piezoelectric layer

2.1 Constitutive relations

This work extends the framework of fluid-saturated porous piezothermoelasticity by incorporating the nonlocal elasticity theory proposed by Eringen [37]. We consider a porous piezoelectric medium saturated with fluid, occupying a domain $\mathcal{V}$ within the spatial set $\aleph$, enclosed by the outer boundary $\Re$ and an internal boundary Ξ. A material point is described by its reference coordinates X_i and its current coordinates x_i, corresponding to the undeformed and deformed configurations, respectively. The solid-phase displacement field is therefore defined as

$$v_i = X_i - x_i.$$

The associated Lagrangian strain measure is written in the standard form

$$\Gamma_{ij} = \tfrac{1}{2}\left(v_{i,j} + v_{j,i}\right).$$

The divergence operators acting on the displacement fields of both the solid and fluid constituents are then introduced as $\Gamma_s = \nabla \cdot \vec{v}$ and $\Gamma^* = \nabla \cdot \vec{V}$, respectively. The fundamental variables at positions $\vec{\alpha}$ and $\vec{\alpha'}$ are further articulated to provide a comprehensive understanding of the material's behavior under these conditions as

$$\mathcal{Y} = \{\Gamma_{ij}(\vec{\alpha}), \Gamma^*(\vec{\alpha}), E_i(\vec{\alpha}), E^*_i(\vec{\alpha})\}, \tag{1}$$

$$\mathcal{Y}' = \left\{\Gamma_{ij}(\vec{\alpha'}), \Gamma^*(\vec{\alpha'}), E_i(\vec{\alpha'}), E^*_i(\vec{\alpha'})\right\}. \tag{2}$$

ARTICLE IN PRESS

The strain energy $\mathcal{U}$ is formulated as

$$\left.\begin{aligned}2\mathcal{U} &= \mathcal{C}_{ijkl}(\vec{\alpha},\vec{\alpha'})\Gamma_{ij}(\vec{\alpha})\Gamma_{kl}(\vec{\alpha'}) + \mathcal{M}_{ij}(\vec{\alpha},\vec{\alpha'})\big[\Gamma_{ij}(\vec{\alpha})\Gamma^*(\vec{\alpha'}) + \Gamma_{ij}(\vec{\alpha'})\Gamma^*(\vec{\alpha})\big]\\ &- \mathcal{E}_{ijk}(\vec{\alpha},\vec{\alpha'})\big[\Gamma_{ij}(\vec{\alpha})E_k(\vec{\alpha'}) + \Gamma_{ij}(\vec{\alpha'})E_k(\vec{\alpha})\big] - \chi_{ijk}(\vec{\alpha},\vec{\alpha'})\big[\Gamma_{ij}(\vec{\alpha})E^*_k(\vec{\alpha'}) + \Gamma_{ij}(\vec{\alpha'})E^*_k(\vec{\alpha})\big]\\ &+ \mathcal{R}(\vec{\alpha},\vec{\alpha'})\Gamma^*(\vec{\alpha})\Gamma^*(\vec{\alpha'}) - \chi^*_i(\vec{\alpha},\vec{\alpha'})\big[\Gamma^*(\vec{\alpha})E_i(\vec{\alpha'}) + \Gamma^*(\vec{\alpha'})E_i(\vec{\alpha})\big]\\ &- \mathcal{E}^*_i(\vec{\alpha},\vec{\alpha'})\big[\Gamma^*(\vec{\alpha})E^*_i(\vec{\alpha'}) + \Gamma^*(\vec{\alpha'})E^*_i(\vec{\alpha})\big] - \mathcal{A}_{ij}(\vec{\alpha},\vec{\alpha'})\big[E_i(\vec{\alpha})E^*_j(\vec{\alpha'}) + E_i(\vec{\alpha'})E^*_j(\vec{\alpha})\big]\\ &- \varsigma_{ij}(\vec{\alpha},\vec{\alpha'})E_i(\vec{\alpha})E_j(\vec{\alpha'}) - \varsigma^*_{ij}(\vec{\alpha},\vec{\alpha'})E^*_i(\vec{\alpha})E^*_j(\vec{\alpha'}).\end{aligned}\right\} \tag{3}$$

The constitutive coefficients incorporate the following symmetries

$$\left.\begin{aligned}&\mathcal{C}_{ijkl}(\vec{\alpha},\vec{\alpha'}) = \mathcal{C}_{klij}(\vec{\alpha},\vec{\alpha'}) = \mathcal{C}_{jikl}(\vec{\alpha},\vec{\alpha'})\ ,\ \mathcal{E}_{ijk}(\vec{\alpha},\vec{\alpha'}) = \mathcal{E}_{jik}(\vec{\alpha},\vec{\alpha'})\ ,\ \chi_{ijk}(\vec{\alpha},\vec{\alpha'}) = \chi_{jik}(\vec{\alpha},\vec{\alpha'})\ ,\\ &\mathcal{M}_{ij}(\vec{\alpha},\vec{\alpha'}) = \mathcal{M}_{ji}(\vec{\alpha},\vec{\alpha'})\ ,\ \varsigma_{ij}(\vec{\alpha},\vec{\alpha'}) = \varsigma_{ji}(\vec{\alpha},\vec{\alpha'})\ ,\mathcal{A}_{ij}(\vec{\alpha},\vec{\alpha'}) = \mathcal{A}_{ji}(\vec{\alpha},\vec{\alpha'}),\ \ \varsigma^*_{ij}(\vec{\alpha},\vec{\alpha'}) = \varsigma^*_{ji}(\vec{\alpha},\vec{\alpha'})\end{aligned}\right\}. \tag{4}$$

The constitutive relations are obtained with the help of the following equation obtained from Eringen [56]

$$\eta = \int_{\mathcal{V}} \left[\frac{\partial \mathcal{U}}{\partial \mathcal{Y}} + \left(\frac{\partial \mathcal{U}}{\partial \mathcal{Y}'}\right)^b\right] d\mathcal{V}(\vec{\alpha'}), \tag{5}$$

where the superscript b indicates that the corresponding quantity remains invariant under the interchange of $\vec{\alpha}$ and $\vec{\alpha}'$. Let $\eta = \{\Upsilon_{ij},\ \Upsilon^*,\ -D_i,\ -D^*_i,\}$ denote the ordered collection associated with equation (1). Invoking equations (1)–(5), the set η can be expressed in the following mathematical form:

$$\Upsilon_{ij} = \int_{\mathcal{V}} \big[\mathcal{C}_{ijkl}(\vec{\alpha},\vec{\alpha'})\Gamma_{kl}(\vec{\alpha'}) + \mathcal{M}_{ij}(\vec{\alpha},\vec{\alpha'})\Gamma^*(\vec{\alpha'}) - \mathcal{E}_{ijk}(\vec{\alpha},\vec{\alpha'})E_k(\vec{\alpha'}) - \chi_{ijk}(\vec{\alpha},\vec{\alpha'})E^*_k(\vec{\alpha'})\big] d\mathcal{V}(\vec{\alpha'}), \tag{6}$$

$$\Upsilon^* = \int_{\mathcal{V}} \big[\mathcal{M}_{ij}(\vec{\alpha},\vec{\alpha'})\Gamma_{ij}(\vec{\alpha'}) + \mathcal{R}(\vec{\alpha},\vec{\alpha'})\Gamma^*(\vec{\alpha'}) - \chi^*_i(\vec{\alpha},\vec{\alpha'})E_i(\vec{\alpha'}) - \mathcal{E}^*_i(\vec{\alpha},\vec{\alpha'})E^*_i(\vec{\alpha'})\big] d\mathcal{V}(\vec{\alpha'}), \tag{7}$$

$$D_i = \int_{\mathcal{V}} \big[\mathcal{E}_{ijk}(\vec{\alpha},\vec{\alpha'})\Gamma_{kj}(\vec{\alpha'}) + \chi^*_i(\vec{\alpha},\vec{\alpha'})\Gamma^*(\vec{\alpha'}) + \varsigma_{ij}(\vec{\alpha},\vec{\alpha'})E_j(\vec{\alpha'}) + \mathcal{A}_{ij}(\vec{\alpha},\vec{\alpha'})E^*_j(\vec{\alpha'})\big] d\mathcal{V}(\vec{\alpha'}), \tag{8}$$

$$D^*_i = \int_{\mathcal{V}} \big[\chi_{ijk}(\vec{\alpha},\vec{\alpha'})\Gamma_{kj}(\vec{\alpha'}) + \mathcal{E}^*_i(\vec{\alpha},\vec{\alpha'})\Gamma^*(\vec{\alpha'}) + \mathcal{A}_{ij}(\vec{\alpha},\vec{\alpha'})\mathcal{E}_j(\vec{\alpha'}) + \varsigma^*_{ij}(\vec{\alpha},\vec{\alpha'})E^*_j(\vec{\alpha'})\big] d\mathcal{V}(\vec{\alpha'}). \tag{9}$$

The constitutive coefficients $\mathcal{C}_{ijkl}$, $\mathcal{E}_{ijk}$, χ_{ijk}, $\mathcal{M}_{ij}$, ς_{ij}, $\mathcal{A}_{ij}$, and ς^*_{ij} are functions of $\tilde{\alpha} = |\vec{\alpha} - \vec{\alpha'}|$. The constitutive relationships (6)-(9) turn into

$$\Upsilon_{ij} = \int_{\mathcal{V}} \big[\mathcal{C}_{ijkl}(\tilde{\alpha})\Gamma_{kl}(\vec{\alpha'}) + \mathcal{M}_{ij}(\tilde{\alpha})\Gamma^*(\vec{\alpha'}) - \mathcal{E}_{ijk}(\tilde{\alpha})E_k(\vec{\alpha'}) - \chi_{ijk}(\tilde{\alpha})E^*_k(\vec{\alpha'})(\vec{\alpha'})\big] d\mathcal{V}(\vec{\alpha'}), \tag{10}$$

$$\Upsilon^* = \int_{\mathcal{V}} \big[\mathcal{M}_{ij}(\tilde{\alpha})\Gamma_{ij}(\vec{\alpha'}) + \mathcal{R}(\tilde{\alpha})\Gamma^*(\vec{\alpha'}) - \chi^*_i(\tilde{\alpha})E_i(\vec{\alpha'}) - \mathcal{E}^*_i(\tilde{\alpha})E^*_i\big] d\mathcal{V}(\vec{\alpha'}), \tag{11}$$

$$D_i = \int_{\mathcal{V}} \big[\mathcal{E}_{ijk}(\tilde{\alpha})\Gamma_{kj}(\vec{\alpha'}) + \chi^*_i(\tilde{\alpha})\Gamma^*(\vec{\alpha'}) + \varsigma_{ij}(\tilde{\alpha})E_j(\vec{\alpha'}) + \mathcal{A}_{ij}(\tilde{\alpha})E^*_j(\vec{\alpha'})\big] d\mathcal{V}(\vec{\alpha'}), \tag{12}$$

$$D^*_i = \int_{\mathcal{V}} \big[\chi_{ijk}(\tilde{\alpha})\Gamma_{kj}(\vec{\alpha'}) + \mathcal{E}^*_i(\tilde{\alpha})\Gamma^*(\vec{\alpha'}) + \mathcal{A}_{ij}(\tilde{\alpha})E_j(\vec{\alpha'}) + \varsigma^*_{ij}(\tilde{\alpha})\mathcal{E}^*_j(\vec{\alpha'})\big] d\mathcal{V}(\vec{\alpha'}). \tag{13}$$

In a nonlocal medium, the influence exerted by a material point diminishes as the separation from the reference position grows. This reduction arises from the gradual fading of intermolecular interactions over larger spatial gaps. Consequently, the associated constitutive coefficient decreases monotonically with increasing distance; in other words, as the gap between two points expands, the contribution of the surrounding continuum to the response at the reference point becomes progressively weaker. For example, when the distance becomes large, one observes that

ARTICLE IN PRESS

ARTICLE IN PRESS

$$\lim_{\tilde{\mathcal{L}}^* \to \infty} d(\tilde{\mathcal{L}}^*) \to 0.$$

At the coincident position $\vec{\alpha} = \vec{\alpha}'$, where each constitutive coefficient reaches its peak magnitude, a clear correspondence arises between the nonlocal elastic parameters and their classical (local) counterparts. This connection can be written as

$$\frac{\mathcal{C}_{ijkl}(\tilde{\alpha})}{\hat{\mathcal{C}}_{ijkl}} = \frac{\mathcal{E}_{ijk}(\tilde{\alpha})}{\hat{\mathcal{E}}_{ijk}} = \frac{\chi_{ijk}(\tilde{\alpha})}{\hat{\chi}_{ijk}} = \frac{\mathcal{M}_{ij}(\tilde{\alpha})}{\hat{\mathcal{M}}_{ij}} = \frac{\varsigma_{ij}(\tilde{\alpha})}{\hat{\varsigma}_{ij}} = \frac{\mathcal{A}_{ij}(\tilde{\alpha})}{\hat{\mathcal{A}}_{ij}} = \frac{\varsigma^*_{ij}(\tilde{\alpha})}{\hat{\varsigma}^*_{ij}}, \tag{14}$$

where $\hat{\mathcal{C}}_{ijkl}$, $\hat{\mathcal{E}}_{ijk}$, $\hat{\chi}_{ijk}$, $\hat{\mathcal{M}}_{ij}$, $\hat{\varsigma}_{ij}$, $\hat{\mathcal{A}}_{ij}$, and $\hat{\varsigma}^*_{ij}$ are material parameters.

The nonlocal attenuation kernel $\Pi(\tilde{\alpha})$ satisfies the normalization condition

$$\int_{\mathcal{V}} \Pi(\tilde{\alpha})\, d\mathcal{V} = 1. \tag{15}$$

Following the formulation proposed by Eringen and Wegner [57], the kernel is further constrained by

$$\left(1 - \Gamma^2 \nabla^2\right) \Pi = \delta(\tilde{\alpha}), \tag{16}$$

where ∇^2 denotes the Laplacian operator, and the parameter $\varepsilon_0 (<< 1)$ represents the intrinsic nonlocal scale, defined through $\varepsilon_0 = \varepsilon_1 l_e$ with ε_1 being a material-dependent constant and l_e the internal characteristic length.

To simplify the complex integral constitutive relations (equations (10)-(13)) into a more tractable differential form, Eringen's differential constitutive model is employed. This is achieved by applying the differential operator $\left(1 - \varepsilon_0^2 \nabla^2\right)$ to both sides of the integral equations and utilizing the property of the Dirac delta function $\delta(\tilde{\alpha})$ in conjunction with the kernel constraint provided by equation (16). This mathematical manipulation converts the long-range inter-atomic interactions into an equivalent local relationship modified by the nonlocal differential operator.

$$\left(1 - \varepsilon_0^2 \nabla^2\right) \Upsilon^{nl}_{ij} = \Upsilon^{l}_{ij} = \mathcal{C}_{ijkl}\Gamma_{kl}(\tilde{\alpha}) + \mathcal{M}_{ij}\Gamma^*(\tilde{\alpha}) - \mathcal{E}_{kij}E_k(\tilde{\alpha}) - \chi_{kij}E^*_k(\tilde{\alpha}), \tag{17}$$

$$\left(1 - \varepsilon_0^2 \nabla^2\right) \Upsilon^{*^{nl}} = \Upsilon^{*^{l}} = \mathcal{M}_{ij}\Gamma_{ij}(\tilde{\alpha}) + \mathcal{R}\Gamma^*(\tilde{\alpha}) - \chi^*_i E_i(\tilde{\alpha}) - \mathcal{E}^*_i E^*_i(\tilde{\alpha}), \tag{18}$$

$$\left(1 - \varepsilon_0^2 \nabla^2\right) D_i = \mathcal{D}^{le}_i = \mathcal{E}_{ijk}\Gamma_{jk}(\tilde{\alpha}) + \chi^*_i\Gamma^*(\tilde{\alpha}) + \varsigma_{ij}E_j(\tilde{\alpha}) + \mathcal{A}_{ij}E^*_j(\tilde{\alpha}), \tag{19}$$

$$\left(1 - \varepsilon_0^2 \nabla^2\right) D^*_i = \mathcal{D}^{*^{le}}_i = \chi_{ijk}\Gamma_{jk}(\tilde{\alpha}) + \mathcal{E}^*_i\Gamma^*(\tilde{\alpha}) + \mathcal{A}_{ij}E_j(\tilde{\alpha}) + \varsigma^*_{ij}E^*_j(\tilde{\alpha}), \tag{20}$$

where $\varrho = (1 - f)\varrho_s + f\varrho_f$. Here, $\mathcal{C}_{ijkl}$ are the elastic constants of the solid phase which are positive definite in the sense that $\mathcal{C}_{ijkl}\Gamma_{ij}\Gamma_{kl} > 0$. $\mathcal{M}_{ij}$ represent the parameters which deal with the coupling between the solid and fluid phases of the porous aggregate. $\mathcal{E}_{ijk}$ are the piezoelectric moduli tensor components for the solid phase. These constants exhibit symmetry in indices j and k. $\mathcal{R}$ measures the pressure to be exerted on the fluid to push its unit volume into the porous matrix. $\mathcal{E}^*_i$ indicate the piezoelectric coefficient for the fluid phase. The coefficients χ_{ijk} quantify the solid–fluid electromechanical coupling. They measure how deformation of the solid skeleton influences the electric field within the pore fluid and, conversely, how the fluid-phase electric field contributes to the total stress. Physically, χ_{ijk} represents the redistribution of polarization and charge transport across the solid–fluid interface under mechanical loading. Similarly, the coefficients $\mathcal{A}_{ij}$ represent the dielectric coupling between the solid and fluid phases. They capture how the electric displacement in the fluid is affected by the electric field in the solid matrix and vice versa. In saturated porous composites, A_{ij} depends on pore geometry, fluid permittivity, and the connectivity of the fluid network.

Under the quasi-static approximation, the electric field can be obtained from scalar electric potentials, Φ and Φ^*, as

$$E_k = -\Phi_{,k}\ ,\ E^*_k = -\Phi^*_{,k}. \tag{21}$$

Equations (17)-(20) represent the nonlocal stress-strain relation for nonlocal porous piezoelectric material.

ARTICLE IN PRESS

3. Problem formulation and geometrical set up

Figure 1 illustrates the physical configuration considered in this study, where a moving line load L_0 travels with a constant speed $\mathcal{V}_0$ across an irregular, transversely isotropic, nonlocal porous piezoelectric layer of thickness H. The upper boundary of the layer is characterized by a friction coefficient $\mathcal{R}_0$. A Cartesian coordinate system $Oxyz$ is adopted such that the z–axis points vertically downward (representing depth), while the x–axis coincides with the direction of motion of the applied load. The origin is positioned at the midpoint of the irregularity span, as indicated in Figure 1.

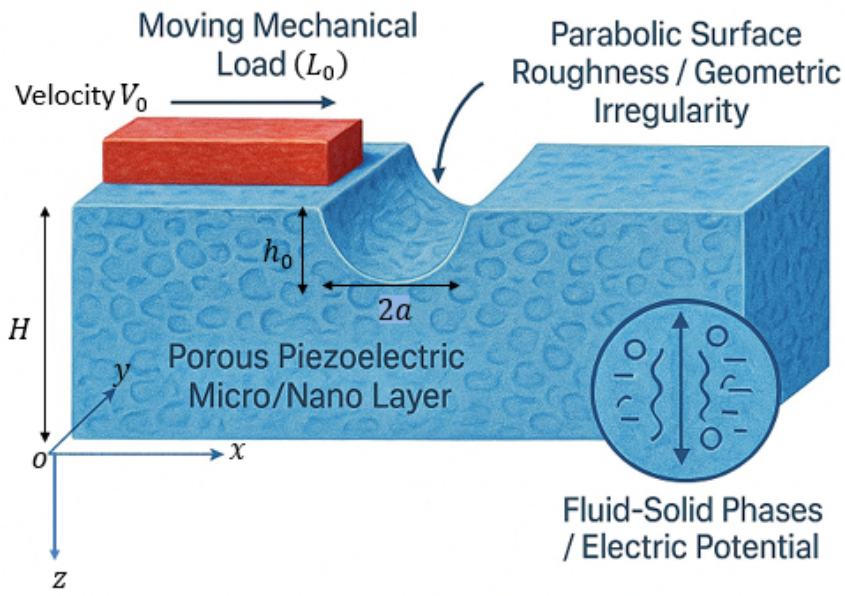


Figure 1. Geometric Configuration of the Problem

To incorporate the surface imperfection, the top boundary is modeled with a parabolic profile. Hence, the irregular surface geometry with total span $2a$ and maximum indentation depth h_0 is described by

$$z = \epsilon_0 \, f(x), \tag{22}$$

where

$$f(x) = \begin{cases} 0, & |x| > a, \\ \dfrac{2}{a}\left(a^2 - x^2\right), & -a \le x \le a. \end{cases}$$

Equation (22) therefore characterizes the perturbed upper boundary. The dimensionless perturbation parameter is defined as $\epsilon_0 = h_0/(2a)$, satisfying $0 < \epsilon_0 < 1$.

4. Solution methodology

4.1 *Wave dynamics of nonlocal porous piezoelectric layer (NPPEL)*

In the absence of body forces and dissipative effects, the governing equations of motion for the nonlocal porous piezoelectric material take the form [58]

$$\begin{aligned} \Upsilon^{l}_{ij,j} &= (1 - \varepsilon_0^2 \nabla^2)\left((\varrho_{11})_{ij}\ddot{v}_i + (\varrho_{12})_{ij}\ddot{v}^*_i\right), \\ \Upsilon^{l^*}_{,i} &= (1 - \varepsilon_0^2 \nabla^2)\left((\varrho_{12})_{ij}\ddot{v}_i + (\varrho_{22})_{ij}\ddot{v}^*_i\right), \qquad (i,j = 1,2,3) \end{aligned} \tag{23}$$

where the dynamic mass coefficients $(\varrho_{11})_{ij}$, $(\varrho_{12})_{ij}$, and $(\varrho_{22})_{ij}$ satisfy the physical assumptions: $(\varrho_{11})_{ij} > 0$, $(\varrho_{22})_{ij} > 0$, $(\varrho_{12})_{ij} \le 0$, and $(\varrho_{11})_{ij}(\varrho_{22})_{ij} - (\varrho_{12})^2_{ij} > 0$. These parameters are related

ARTICLE IN PRESS

to the solid density ϱ_s, fluid density ϱ_f, and porosity f through the following established relations: $(\varrho_{11})_{ij}+(\varrho_{12})_{ij} = (1-f)\varrho_s\delta_{ij}$, $(\varrho_{12})_{ij}+(\varrho_{22})_{ij} = f\varrho_f\delta_{ij}$, and $\varrho\delta_{ij} = (\varrho_{11})_{ij}+2(\varrho_{12})_{ij}+(\varrho_{22})_{ij}$.

The electro-dynamic Maxwell relations governing a porous piezoelectric medium, upon neglecting the displacement electric current, reduce to [58]

$$\begin{aligned} &D_{i,i} = 0, \\ &D^*_{i,i} = 0. \qquad (i = 1,2,3) \end{aligned} \tag{24}$$

To facilitate the solution, the general local constitutive relations Υ^l_{ij}, Υ^{*^l}, D^l_i, and $D^{*^l}_i$, as expressed in equations (17)-(20) are specialized for a transversely isotropic porous piezoelectric solid [58]:

$$\left.\begin{aligned}
&(1-\varepsilon_0^2\nabla^2)\Upsilon^{nl}_{xx} = \Upsilon^l_{xx} = \mathcal{C}_{11}\Gamma_{xx}+\mathcal{C}_{12}\Gamma_{yy}+\mathcal{C}_{13}\Gamma_{zz}+M_{11}\Gamma^*-\mathcal{E}_{31}E_z-\chi_{31}E^*_z,\\
&(1-\varepsilon_0^2\nabla^2)\Upsilon^{nl}_{yy} = \Upsilon^l_{yy} = \mathcal{C}_{12}\Gamma_{xx}+\mathcal{C}_{11}\Gamma_{yy}+\mathcal{C}_{13}\Gamma_{zz}+M_{11}\Gamma^*-\mathcal{E}_{31}E_z-\chi_{31}E^*_z,\\
&(1-\varepsilon_0^2\nabla^2)\Upsilon^{nl}_{zz} = \Upsilon^l_{zz} = \mathcal{C}_{13}\Gamma_{xx}+\mathcal{C}_{13}\Gamma_{yy}+\mathcal{C}_{33}\Gamma_{zz}+M_{33}\Gamma^*-\mathcal{E}_{33}E_z-\chi_{33}E^*_z,\\
&(1-\varepsilon_0^2\nabla^2)\Upsilon^{nl}_{yz} = \Upsilon^l_{yz} = 2\mathcal{C}_{44}\Gamma_{yz}-\mathcal{E}_{15}E_y-\chi_{15}E^*_y,\\
&(1-\varepsilon_0^2\nabla^2)\Upsilon^{nl}_{zx} = \Upsilon^l_{zx} = 2\mathcal{C}_{44}\Gamma_{zx}-\mathcal{E}_{15}E_x-\chi_{15}E^*_x,\\
&(1-\varepsilon_0^2\nabla^2)\Upsilon^{nl}_{xy} = \Upsilon^l_{xy} = 2\mathcal{C}_{44}\Gamma_{xy},\\
&(1-\varepsilon_0^2\nabla^2)\Upsilon^{*^{nl}} = \Upsilon^{*^l} = \mathcal{M}_{11}\Gamma_{xx}+\mathcal{M}_{11}\Gamma_{yy}+\mathcal{M}_{33}\Gamma_{zz}+\mathcal{R}\Gamma^*-\chi^*_3E_z-\mathcal{E}^*_3E^*_z,\\
&(1-\varepsilon_0^2\nabla^2)D^{nl}_x = D^l_x = 2\mathcal{E}_{15}\Gamma_{zx}+\varsigma_{11}E_x+\mathcal{A}_{11}E^*_x,\\
&(1-\varepsilon_0^2\nabla^2)D^{nl}_y = D^l_y = 2\mathcal{E}_{15}\Gamma_{yz}+\varsigma_{11}E_y+\mathcal{A}_{11}E^*_y,\\
&(1-\varepsilon_0^2\nabla^2)D^{nl}_z = D^l_z = \mathcal{E}_{31}\Gamma_{xx}+\mathcal{E}_{31}\Gamma_{yy}+\mathcal{E}_{33}\Gamma_{zz}+\chi^*_3\Gamma^*+\varsigma_{33}E_z+\mathcal{A}_{33}E^*_z,\\
&(1-\varepsilon_0^2\nabla^2)D^{*^{nl}}_x = D^{*^l}_x = 2\chi_{15}\Gamma_{zx}+\mathcal{A}_{11}E_x+\varsigma^*_{11}E^*_x,\\
&(1-\varepsilon_0^2\nabla^2)D^{*^{nl}}_y = D^{*^l}_y = 2\chi_{15}\Gamma_{yx}+\mathcal{A}_{11}E_y+\varsigma^*_{11}E^*_y,\\
&(1-\varepsilon_0^2\nabla^2)D^{*^{nl}}_z = D^{*^l}_z = \chi_{31}\Gamma_{xx}+\chi_{31}\Gamma_{yy}+\chi_{33}\Gamma_{zz}+\mathcal{E}^*_3\Gamma^*+\mathcal{A}_{33}E_z+\varsigma^*_{33}E^*_z.
\end{aligned}\right\} \tag{25}$$

The connections between the strain measures and the mechanical displacement fields, together with the relations linking the electric field intensities to their corresponding electric potentials in both solid and fluid phases, are expressed as

$$\Gamma_{ij} = \tfrac{1}{2}\left(v_{i,j}+v_{j,i}\right), \qquad \Gamma^* = v_{k,k}, \qquad E_i = -\Phi_{,i}, \qquad E^*_i = -\Phi^*_{,i}. \tag{26}$$

For a plane–strain setting restricted to the xz–plane, the displacement and potential fields are specified in the form

$$\begin{aligned} &v_1 = v_1(x,z,t), \qquad v_2 = 0, \qquad v_3 = v_3(x,z,t), \qquad \Phi = \Phi(x,z,t), \\ &\Phi^* = \Phi^*(x,z,t), \qquad \text{with} \quad \frac{\partial}{\partial y} = 0. \end{aligned} \tag{27}$$

The final set of coupled partial differential equations is obtained by substituting the reduced local constitutive relations (25), along with the kinematic and electric potential relations (26) and (27), into the equations of motion (23) and the Maxwell equation (24). After extensive algebraic manipulation and applying the plane-strain condition ($\partial/\partial y = 0$), the four coupled field equations for the displacement components (v_1, v_3) and the electric potentials (Φ, Φ^*) in the xz-plane are derived as follows:

$$\begin{aligned}
&\left(\mathcal{C}_{11}-\frac{(\varrho_{12})_{11}}{(\varrho_{22})_{11}}\mathcal{M}_{11}\right)\frac{\partial^2 v_1}{\partial x^2}+\left(\mathcal{C}_{44}+\mathcal{C}_{13}-\frac{(\varrho_{12})_{11}}{(\varrho_{22})_{11}}\mathcal{M}_{33}\right)\frac{\partial^2 v_3}{\partial x\partial z}\\
&+\left(\mathcal{E}_{31}+\mathcal{E}_{15}-\chi^*_3\frac{(\varrho_{12})_{11}}{(\varrho_{22})_{11}}\right)\frac{\partial^2\Phi}{\partial x\partial z}+\left(\chi_{31}+\chi_{15}-\mathcal{E}^*_3\frac{(\varrho_{12})_{11}}{(\varrho_{22})_{11}}\right)\frac{\partial^2\Phi^*}{\partial x\partial z}\\
&+\mathcal{C}_{44}\frac{\partial^2 v_1}{\partial z^2}+d'_{11}\varepsilon_0^2\frac{\partial^4 v_1}{\partial t^2\partial x^2}+d'_{11}\varepsilon_0^2\frac{\partial^4 v_1}{\partial t^2\partial z^2}-d'_{11}\frac{\partial^2 v_1}{\partial t^2}=0,
\end{aligned} \tag{28}$$

ARTICLE IN PRESS

$$\left(\mathcal{C}_{33}-\frac{(\varrho_{12})_{33}}{(\varrho_{22})_{33}}\mathcal{M}_{33}\right)\frac{\partial^2 v_3}{\partial z^2}+\left(\mathcal{C}_{44}+\mathcal{C}_{13}-\frac{(\varrho_{12})_{33}}{(\varrho_{22})_{33}}\mathcal{M}_{11}\right)\frac{\partial^2 v_1}{\partial x\partial z}+\left(\mathcal{E}_{33}-\chi_3^*\frac{(\varrho_{12})_{33}}{(\varrho_{22})_{33}}\right)\frac{\partial^2\phi}{\partial z^2}$$
$$+\mathcal{C}_{44}\frac{\partial^2 v_3}{\partial x^2}+\left(\chi_{33}-\frac{(\varrho_{12})_{33}}{(\varrho_{22})_{33}}\mathcal{E}_3^*\right)\frac{\partial^2\Phi^*}{\partial z^2}+\chi_{15}\frac{\partial^2\Phi^*}{\partial x^2}+d'_{33}\varepsilon_0^2\frac{\partial^4 v_3}{\partial t^2\partial x^2}+d'_{33}\varepsilon_0^2\frac{\partial^4 v_3}{\partial t^2\partial z^2}-d'_{33}\frac{\partial^2 v_3}{\partial t^2}=0, \tag{29}$$

$$\mathcal{E}_{15}\left(\frac{\partial^2 v_3}{\partial x^2}+\frac{\partial^2 v_1}{\partial z\partial x}\right)-\varsigma_{11}\frac{\partial^2\Phi}{\partial x^2}-\mathcal{A}_{11}\frac{\partial^2\Phi^*}{\partial x^2}+\mathcal{E}_{31}\frac{\partial^2 v_1}{\partial z\partial x}+\mathcal{E}_{33}\frac{\partial^2 v_3}{\partial z^2}-\varsigma_{33}\frac{\partial^2\Phi}{\partial z^2}-\mathcal{A}_{33}\frac{\partial^2\Phi^*}{\partial z^2}=0, \tag{30}$$

$$\chi_{15}\left(\frac{\partial^2 v_3}{\partial x^2}+\frac{\partial^2 v_1}{\partial z\partial x}\right)-\mathcal{A}_{11}\frac{\partial^2\Phi}{\partial x^2}-\varsigma_{11}^*\frac{\partial^2\Phi^*}{\partial x^2}+\chi_{31}\frac{\partial^2 v_1}{\partial z\partial x}+\chi_{33}\frac{\partial^2 v_3}{\partial z^2}-\mathcal{A}_{33}\frac{\partial^2\Phi}{\partial z^2}-\varsigma_{33}^*\frac{\partial^2\Phi^*}{\partial z^2}=0, \tag{31}$$

where $d'_{11}=(\varrho_{11})_{11}-\frac{(\varrho_{12})_{11}^2}{(\varrho_{22})_{11}}$ and $d'_{33}=(\varrho_{11})_{33}-\frac{(\varrho_{12})_{33}^2}{(\varrho_{22})_{33}}$.
The solutions of the equations (28)-(31) are assumed in the following formula,

$$v_1=\int_0^\infty\left(A\cos k(x-\mathcal{V}_0t)+B\sin k(x-\mathcal{V}_0t)\right)e^{-k\nu z}\,dk, \tag{32}$$

$$v_3=\int_0^\infty\left(C\cos k(x-\mathcal{V}_0t)+D\sin k(x-\mathcal{V}_0t)\right)e^{-k\nu z}\,dk, \tag{33}$$

$$\Phi=\int_0^\infty\left(\overline{A}\cos k(x-\mathcal{V}_0t)+\overline{B}\sin k(x-\mathcal{V}_0t)\right)e^{-k\nu z}\,dk, \tag{34}$$

$$\Phi^*=\int_0^\infty\left(\overline{C}\cos k(x-\mathcal{V}_0t)+\overline{D}\sin k(x-\mathcal{V}_0t)\right)e^{-k\nu z}\,dk, \tag{35}$$

where A,B,C,D together with $\overline{A},\overline{B},\overline{C}$ and $\overline{D}$ are undetermined constants, and ν denotes a positive real, dimensionless quantity that remains unaffected by the choice of the wavenumber k.
Now substituting the aforementioned equations into the equations (28)-(31), we obtain the following system of simultaneous equations:

$$\begin{aligned}\left(n_2+n_1\nu^2\right)A-m_2q\overline{D}-m_3\nu\overline{B}-m_4\nu\overline{D}=0,\\ \left(n_2+n_1\nu^2\right)B+m_2\nu+m_3\nu\overline{A}+m_4\nu\overline{C}=0,\end{aligned} \tag{36}$$

$$\begin{aligned}-m_5\nu B+\left(n_3+n_4\nu^2\right)C+\left(m_7\nu^2-\mathcal{E}_{15}\right)\overline{A}+\left(m_8\nu^2-\chi_{15}\right)\overline{C}=0,\\ m_5\nu A+\left(n_3+n_4\nu^2\right)D+\left(m_7q^2-\mathcal{E}_{15}\right)\overline{B}+\left(m_8\nu^2-\chi_{15}\right)\overline{D}=0,\end{aligned} \tag{37}$$

$$\begin{aligned}-m_9\nu B-\left(\mathcal{E}_{15}-\mathcal{E}_{33}\nu^2\right)C+\left(\varsigma_{11}-\varsigma_{33}\nu^2\right)\overline{A}+\left(\mathcal{A}_{11}-\mathcal{A}_{33}\nu^2\right)\overline{C}=0,\\ m_9\nu A-\left(\mathcal{E}_{15}-\mathcal{E}_{33}\nu^2\right)D+\left(\varsigma_{11}-\varsigma_{33}\nu^2\right)\overline{B}+\left(\mathcal{A}_{11}-\mathcal{A}_{33}\nu^2\right)\overline{D}=0,\end{aligned} \tag{38}$$

$$\begin{aligned}-m_{10}\nu B-\left(\chi_{15}-\chi_{33}\nu^2\right)C+\left(\mathcal{A}_{11}-\mathcal{A}_{33}\nu^2\right)\overline{A}+\left(\varsigma_{11}^*-\varsigma_{33}^*\nu^2\right)\overline{C}=0,\\ m_{10}\nu A-\left(\chi_{15}-\chi_{33}\nu^2\right)D+\left(\mathcal{A}_{11}-\mathcal{A}_{33}\nu^2\right)\overline{B}+\left(\varsigma_{11}^*-\varsigma_{33}^*\nu^2\right)\overline{D}=0,\end{aligned} \tag{39}$$

where $m_i(i=1,2,...10)$ and $n_i(i=1,2,3,4)$ are defined in Appendix A.
Equations (36)-(39) are consistent if

$$\nu^8\theta_1-\nu^7\theta_2+\nu^6\theta_3-\nu^5\theta_4+\nu^4\theta_5-\nu^3\theta_6+\nu^2\theta_7-\nu\theta_8+\theta_9=0. \tag{40}$$

Upon incorporating equation (40), the system described by (32)–(35) transforms into:

$$\begin{aligned}v_1=\int_0^\infty\left(A_1e^{-k\nu_1z}+A_2e^{-k\nu_2z}+A_3e^{-k\nu_3z}+A_4e^{-k\nu_4z}\right)\cos k(x-\mathcal{V}_0t)\\ +\left(B_1e^{-k\nu_1z}+B_2e^{-k\nu_2z}+B_3e^{-k\nu_3z}+B_4e^{-k\nu_4z}\right)\sin k(x-\mathcal{V}_0t)\,dk,\end{aligned} \tag{41}$$

$$\begin{aligned}v_3=\int_0^\infty\left(\Theta_1^{(1)}B_1e^{-k\nu_1z}+\Theta_2^{(1)}B_2e^{-k\nu_2z}+\Theta_3^{(1)}B_3e^{-k\nu_3z}+\Theta_4^{(1)}B_4e^{-k\nu_4z}\right)\cos k(x-\mathcal{V}_0t)\\ +\left(\Psi_1^{(1)}A_1e^{-k\nu_1z}+\Psi_2^{(1)}A_2e^{-k\nu_2z}+\Psi_3^{(1)}A_3e^{-k\nu_3z}+\Psi_4^{(1)}A_4e^{-k\nu_4z}\right)\sin k(x-\mathcal{V}_0t)\,dk,\end{aligned} \tag{42}$$

ARTICLE IN PRESS

$$\Phi = \int_0^\infty \left(\Theta_1^{(2)} B_1 e^{-k\nu_1 z} + \Theta_2^{(2)} B_2 e^{-k\nu_2 z} + \Theta_3^{(2)} B_3 e^{-k\nu_3 z} + \Theta_4^{(2)} B_4 e^{-k\nu_4 z}\right) \cos k(x - \mathcal{V}_0 t) + \left(\Psi_1^{(2)} A_1 e^{-k\nu_1 z} + \Psi_2^{(2)} A_2 e^{-k\nu_2 z} + \Psi_3^{(2)} A_3 e^{-k\nu_3 z} + \Psi_4^{(2)} A_4 e^{-k\nu_4 z}\right) \sin k(x - \mathcal{V}_0 t)\, dk, \tag{43}$$

$$\Phi^* = \int_0^\infty \left(\Theta_1^{(3)} B_1 e^{-k\nu_1 z} + \Theta_2^{(3)} B_2 e^{-k\nu_2 z} + \Theta_3^{(3)} B_3 e^{-k\nu_3 z} + \Theta_4^{(3)} B_4 e^{-k\nu_4 z}\right) \cos k(x - \mathcal{V}_0 t) + \left(\Psi_1^{(3)} A_1 e^{-k\nu_1 z} + \Psi_2^{(3)} A_2 e^{-k\nu_2 z} + \Psi_3^{(3)} A_3 e^{-k\nu_3 z} + \Psi_4^{(3)} A_4 e^{-k\nu_4 z}\right) \sin k(x - \mathcal{V}_0 t)\, dk. \tag{44}$$

where ν_i, for $i = 1, 2, 3, 4$ are the roots of the equation (40).

5. Boundary conditions and induced stresses

(i) On the perturbed surface $z = \epsilon_0 f(x)$, the influence of the moving load leads to the following boundary conditions:

$$\Upsilon_{zz}^{nl} - \epsilon_0 f' \Upsilon_{zx}^{nl} = -(1 + \varepsilon_0^2 \nabla^2) L_0 \delta(x - \mathcal{V}_0 t), \tag{45}$$

$$\Upsilon_{zx}^{nl} - \epsilon_0 f' \Upsilon_{xx}^{nl} = -(1 + \varepsilon_0^2 \nabla^2) L_0 \mathcal{R}_0 \delta(x - \mathcal{V}_0 t), \tag{46}$$

$$\Phi + \Phi^* = 0, \tag{47}$$

where $\delta(x - \mathcal{V}_0 t)$ denotes the Dirac delta distribution, which may be represented in integral form as

$$\delta(x - \mathcal{V}_0 t) = \frac{1}{\pi} \int_0^\infty \cos[k(x - \mathcal{V}_0 t)]\, dk.$$

(ii) The boundary conditions at the interface $z = H$ are prescribed as

$$\Upsilon_{zz}^{nl} = 0, \tag{48}$$

$$\Upsilon_{zx}^{nl} = 0, \tag{49}$$

$$\Phi + \Phi^* = 0. \tag{50}$$

Due to the non-uniform boundary surface of the considered layered model, the constants A_1, A_2, A_3, A_4, B_1, B_2, B_3 and B_4 are assumed to be the functions of ϵ_0. By expanding these quantities up to the first order of ϵ_0, we obtain

$$\begin{aligned} &A_1 \cong A_{10} + \epsilon_0 A_{11}, A_2 \cong A_{20} + \epsilon_0 A_{21}, A_3 \cong A_{30} + \epsilon_0 A_{31}, A_4 \cong A_{40} + \epsilon_0 A_{41}, \\ &B_1 \cong B_{10} + \epsilon_0 B_{11}, B_2 \cong B_{20} + \epsilon_0 B_{21}, B_3 \cong B_{30} + \epsilon_0 B_{31}, B_4 \cong B_{40} + \epsilon_0 B_{41}, \end{aligned} \tag{51}$$

where A_{ij} and B_{ij} $(i = 1, 2, 3, 4)$ and $(j = 0, 2)$ are undetermined constants.
On solving boundary conditions and with help of aforementioned equations, we obtain

$$\sum_{i=1}^{4} (\mathcal{C}_{13} - \nu_i p_i)\, \beta_i B_{i0} = -\frac{L_0}{k\pi}, \tag{52}$$

$$\sum_{i=1}^{4} -(\mathcal{C}_{13} + \nu_i t_i)\, \beta_i A_{i0} = 0, \tag{53}$$

$$\sum_{i=1}^{4} (r_i - \mathcal{C}_{44}\nu_i)\, \beta_i A_{i0} = -\frac{L_0 \mathcal{R}_0}{k\pi}, \tag{54}$$

$$\sum_{i=1}^{4} -(\mathcal{C}_{44}\nu_i + s_i)\beta_i B_{i0} = 0, \tag{55}$$

$$\sum_{i=1}^{4} \left(\Theta_i^{(2)} + \Theta_i^{(3)}\right) B_{i0} = 0, \tag{56}$$

ARTICLE IN PRESS

ARTICLE IN PRESS

$$\sum_{i=1}^{4}\left(\Psi_i^{(2)}+\Psi_i^{(3)}\right)A_{i0}=0, \tag{57}$$

$$\sum_{i=1}^{4}\left(\mathcal{C}_{13}-\nu_i p_i\right)\beta_i B_{i1}=\sum_{i=1}^{4}\left(\mathcal{C}_{13}-\nu_i p_i\right)\beta_i kf\nu_i B_{i0}+f'\left(r_i-\mathcal{C}_{44}\nu_i\right)\beta_i A_{i0}, \tag{58}$$

$$\sum_{i=1}^{4}\left(\mathcal{C}_{13}+\nu_i t_i\right)\beta_i A_{i1}=\sum_{i=1}^{4}\left(\mathcal{C}_{13}+\nu_i t_i\right)\beta_i kf\nu_i A_{i0}+f'(\mathcal{C}_{44}\nu_i+s_i)\beta_i B_{i0}, \tag{59}$$

$$\sum_{i=1}^{4}\left(r_i-\mathcal{C}_{44}\nu_i\right)\beta_i A_{i1}=\sum_{i=1}^{4}\left(r_i-\mathcal{C}_{44}\nu_i\right)kf\beta_i A_{i0}+f'\left(\mathcal{C}_{11}-w_i\nu_i\right)\beta_i B_{i0}, \tag{60}$$

$$\sum_{i=1}^{4}(\mathcal{C}_{44}\nu_i+s_i)\beta_i B_{i1}=\sum_{i=1}^{4}(\mathcal{C}_{44}\nu_i+s_i)kf\nu_i B_{i0}+f'\left(\mathcal{C}_{11}+y_i\nu i\right)\beta_i A_{i0}, \tag{61}$$

$$\sum_{i=1}^{4}\left(\Theta_i^{(2)}+\Theta_i^{(3)}\right)B_{i1}=\left(\Theta_i^{(2)}+\Theta_i^{(3)}\right)kf\nu_i B_{i0}, \tag{62}$$

$$\sum_{i=1}^{4}\left(\Psi_i^{(2)}+\Psi_i^{(3)}\right)A_{i1}=\left(\Psi_i^{(2)}+\Psi_i^{(3)}\right)kf\nu_i A_{i0}. \tag{63}$$

By solving aforementioned equations, we get

$$\begin{aligned}
&A_{10}=\frac{L_0}{k\pi}W_{10}, A_{20}=\frac{L_0}{k\pi}W_{20}, A_{30}=\frac{L_0}{k\pi}W_{30}, A_{40}=\frac{L_0}{k\pi}W_{40},\\
&A_{11}=\frac{L_0}{k\pi}W_{11}, A_{21}=\frac{L_0}{k\pi}W_{21}, A_{31}=\frac{L_0}{k\pi}W_{31}, A_{41}=\frac{L_0}{k\pi}W_{41},\\
&B_{10}=\frac{L_0}{k\pi}\mathcal{W}_{10}, B_{20}=\frac{L_0}{k\pi}\mathcal{W}_{20}, B_{30}=\frac{L_0}{k\pi}\mathcal{W}_{30}, B_{40}=\frac{L_0}{k\pi}\mathcal{W}_{40},\\
&B_{11}=\frac{L_0}{k\pi}\mathcal{W}_{11}, B_{21}=\frac{L_0}{k\pi}\mathcal{W}_{21}, B_{31}=\frac{L_0}{k\pi}\mathcal{W}_{31}, B_{41}=\frac{L_0}{k\pi}\mathcal{W}_{41},
\end{aligned} \tag{64}$$

where W_{ij} and $\mathcal{W}_{ij}$, $i=1,2$ and $j=0,1$, are obtained by using MATHEMATICA software. After substituting equation (64) into the expression of the displacement components v_1 and v_3, the local shear and normal stresses of the present model due to moving load can be determined by performing integration on the expressions obtained from equation (25) are given by,

$$\frac{\Upsilon_{zx}^{l}}{L_0}=\frac{1}{\pi}\sum_{i=1}^{4}\Big[\frac{\left(r_i-\mathcal{C}_{44}\nu_i\right)\nu_i z W_i}{\nu_i^2 z^2+(x-\mathcal{V}_0 t)^2}-\frac{\left(s_i+\mathcal{C}_{44}\nu_i\right)(x-\mathcal{V}_0 t)\mathcal{W}_i}{\nu_i^2 z^2+(x-\mathcal{V}_0 t)^2}\Big], \tag{65}$$

$$\frac{\Upsilon_{zz}^{l}}{L_0}=\frac{1}{\pi}\sum_{i=1}^{4}\Big[\frac{-(\mathcal{C}_{13}+\nu_i t_i)(x-\mathcal{V}_0 t)W_i}{\nu_i^2 z^2+(x-\mathcal{V}_0 t)^2}+\frac{(\mathcal{C}_{13}-\nu_i p_i)\nu_i z\mathcal{W}_i}{\nu_i^2 z^2+(x-\mathcal{V}_0 t)^2}\Big], \tag{66}$$

where $W_i=W_{i0}+\epsilon_0 W_{i1}$ and $\mathcal{W}_i=\mathcal{W}_{i0}+\epsilon_0\mathcal{W}_{i1}$ for $i=1,2,3,4$.

By combining equations (65) and (66) and adopting a low-order approximation framework, the system simplifies to

$\Upsilon_{zx}^{nl}=(1+\varepsilon_0^2\nabla^2)\Upsilon_{zx}^{l}$ and $\Upsilon_{zz}^{nl}=(1+\varepsilon_0^2\nabla^2)\Upsilon_{zz}^{l}$, the nonlocal stresses of the current model are derived,

$$\Upsilon_{zx}^{nl}=\frac{1}{\pi}\sum_{i=1}^{4}\left\{\frac{\left(r_i-\mathcal{C}_{44}\nu_i\right)}{\nu_i z}-\frac{2\left(r_i-\mathcal{C}_{44}\nu_i\right)}{\nu_i^3 z^3}\varepsilon_0^2+\frac{2\left(r_i-\mathcal{C}_{44}\nu_i\right)}{\nu_i z^3}\varepsilon_0^2\right\}\mathcal{W}_i, \tag{67}$$

$$\Upsilon_{zz}^{nl}=\frac{1}{\pi}\sum_{i=1}^{4}\left\{\frac{(\mathcal{C}_{13}-\nu_i p_i)}{\nu_i z}-\frac{2\left(\mathcal{C}_{13}-\nu_i p_i\right)\nu_i)}{\nu_i^3 z^3}\varepsilon_0^2+\frac{2(\mathcal{C}_{13}-\nu_i p_i)}{\nu_i z^3}\varepsilon_0^2\right\}W_i. \tag{68}$$

6. Validation

Some particular cases are presented in Table 2, which validates the current mathematical model.

ARTICLE IN PRESS

Table 2: Notable cases and their corresponding models.

Case	Condition	Model
1	$\varepsilon_0 = 0, z \to \infty$	This case corresponds to a local porous piezoelectric halfspace. The obtained results show excellent agreement with those reported by Rakshit et al. [21], when the viscosity parameter is neglected.
2	$\varepsilon_0 = 0, z \to \infty$, $\mathcal{M}_{11} = \mathcal{M}_{33} = \mathcal{A}_{11} = \mathcal{A}_{33} = 0$ $\chi_{31} = \chi_{33} = \chi_{15} = \chi_3^* = \mathcal{E}_3^* = \varsigma_{11}^* = \varsigma_{33}^* = 0$	This configuration describes a local piezoelectric halfspace with parabolic irregularity. The findings are consistent with the results of Kumari et al. [59],
3	$\varepsilon_0 = 0, z \to \infty$, $\mathcal{M}_{11} = \mathcal{M}_{33} = \mathcal{A}_{11} = \mathcal{A}_{33} = 0$ $\chi_{31} = \chi_{33} = \chi_{15} = \chi_3^* = \mathcal{E}_3^* = \varsigma_{11}^* = \varsigma_{33}^* = 0$ $\mathcal{C}_{44}{=}\mu, \mathcal{C}_{11}{=}\mathcal{C}_{12}{=}\mathcal{C}_{13}{=}\mathcal{C}_{33}{=}\lambda$	This case corresponds to a isotropic halfspace with irregularity. The resulting model has a perfect validation with those reported by Chattopadhyay et al. [60].
4	$\chi_{31} = \chi_{33} = \chi_{15} = \chi_3^* = \mathcal{E}_3^* = \varsigma_{11}^* = \varsigma_{33}^* = 0$, $\mathcal{C}_{44}{=}\mu$, $\mathcal{C}_{11}{=}\mathcal{C}_{12}{=}\mathcal{C}_{13}{=}\mathcal{C}_{33}{=}\lambda$	This case corresponds to a nonlocal porous layer with parabolic irregularity which is in well agreement with Gupta et al. [45] in the absence of the halfspace and fracture porosity of the double porous layer.

7. Numerical results and discussions

The influence of the frictional coefficient ($\mathcal{R}_0$), the irregularity depth (h_0/a), the irregularity factor (x/a), and the nonlocal parameter (ε_0) on the nonlocal normal stress ($\Upsilon_{zz}^{nl} H/L_0$), shear stress ($\Upsilon_{zx}^{nl} H/L_0$), displacement fields (v_1, v_3), and the electric potentials of the solid (Φ) and fluid (Φ^*) phases of the NPPEL is illustrated through the graphical results presented in Figures 2–5.

The numerical simulations employ the material properties of PZT–5A, with the corresponding constants for the NPPEL adopted from the parameters listed in Table 3.

Table 3: Elastic,piezoelectric, dielectric, and dynamic coefficients of PZT-5A material [61, 62]

Elastic constants (GPa)	Piezoelectric constants (C/m^2)	Dielectric constants $(C^2N^{-1}m^2)\times 10^{-9}$	Dynamic coefficients (kg/m^3)
$\mathcal{C}_{11} = 121$	$\mathcal{E}_{15} = 17.0$	$\varsigma_{11} = 8.1$	$\varrho = 6700$
$\mathcal{C}_{12} = 75.2$	$\mathcal{E}_{31} = -5.4$	$\varsigma_{11} = 7.34$	$(\varrho_{11})_{11} = 4950$
$\mathcal{C}_{13} = 75.2$	$\mathcal{E}_{33} = 12.3$		$(\varrho_{12})_{11} = -1125$
$\mathcal{C}_{33} = 111$	$\chi_{15} = 3.36$		$(\varrho_{22})_{11} = 4800$
$\mathcal{C}_{44} = 21.1$	$\chi_{31} = -0.8$		
	$\chi_{33} = 5.76$		

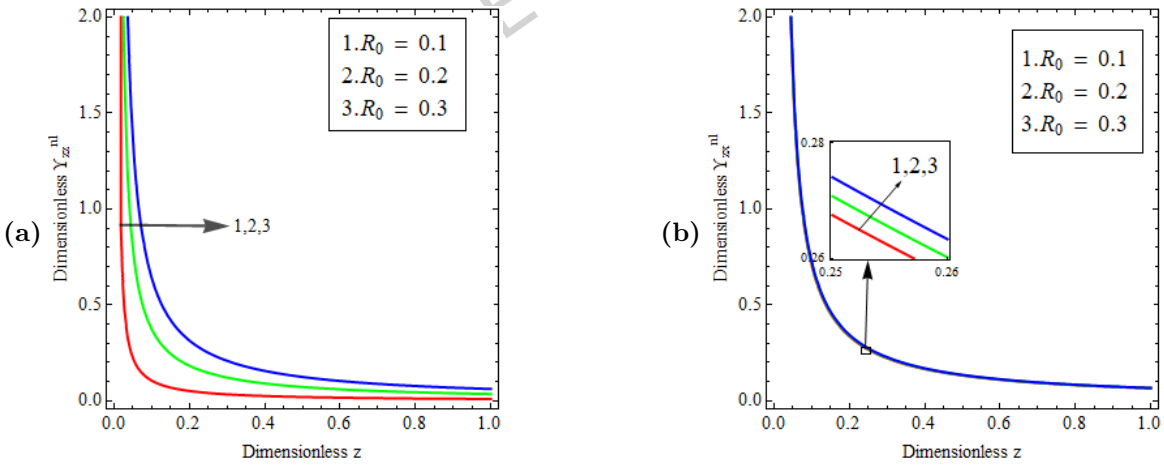
7.1 *Effect of frictional coefficient*

The variation of the nonlocal stresses $\Upsilon_{zz}^{nl} H/L_0$ and $\Upsilon_{zx}^{nl} H/L/L_0$, displacements v_1 and v_3, and the electric potentials Φ and Φ^* with respect to the depth (z/H) for different values of the frictional coefficient $\mathcal{R}_0$ is depicted in Figures 2(a)–2(f). Curves 1, 2, and 3 correspond to $\mathcal{R}_0 = 0.1, 0.2$, and 0.3, respectively. The valid range of R_0 is $[0, 1]$.

Figures 2(a) and 2(b) indicate that an increase in $\mathcal{R}_0$ leads to a rise in the stresses $\Upsilon_{zz}^{nl}H/L_0$ and $\Upsilon_{zx}^{nl}H/L_0$. This trend is consistent with the physical expectation that friction acts opposite to the motion of the applied load, thereby intensifying the stress field. However, in Figure 2(b), the influence of $\mathcal{R}_0$ on $\Upsilon_{zx}^{nl}H/L_0$ is extremely weak, and the curves exhibit slight downward trend near the surface. The distinction between the curves is much more apparent in Figure 2(a) than in Figure 2(b).

In Figure 2(c), the vertical axis representing the horizontal displacement component v_1 carries a negative sign. This negative sign indicates the direction of the displacement (contraction/backward shift) relative to the positive x-axis. As the friction parameter R_0 increases from 0.1 to 0.3, the numerical values move further from zero in the negative direction. Consequently, while the algebraic value decreases, the absolute magnitude $|v_1|$ actually increases. Therefore, both the horizontal displacement (v_1) and the vertical displacement (v_3) exhibit a consistent physical trend: their magnitudes ascend as the friction parameter R_0 increases. The separation between the curves reduces as z approaches unity, implying that the effect of $\mathcal{R}_0$ becomes less dominant at greater depths. In figure 2(d), the spacing between the successive curves remains small, and v_3 tends to flatten as $z \to 1$, suggesting that the vertical displacement approaches a negligible value near the bottom surface.

From Figure 2(e) and 2(f), it is evident that when the friction coefficient increases, the tangential resistance at the upper surface suppresses horizontal deformation of the solid skeleton. This reduction in in-plane strain directly weakens the piezoelectric contribution associated with the solid phase, leading to a decrease in Φ. In contrast, the same friction-induced constraint enhances vertical deformation and pore-fluid dilatation within the porous network. Because the fluid-phase electric potential Φ^* is coupled to the dilatational strain of the fluid and the mixed fluid–solid electromechanical terms, an increase in fluid compression produces a stronger fluid-phase electrical response. This results in an increase in Φ^*. In both cases, the differences among the curves are marginal. Furthermore, as $z \to 1$, the curves become nearly horizontal, indicating that Φ and Φ^* approach very small values near the lower boundary.



7.2 *Effect of irregularity depth*

Figures 3(a)–3(f) illustrate the variation of the quantities $\Upsilon_{zz}^{nl}H/L_0$, $\Upsilon_{zx}^{nl}H/L_0$, v_1, v_3, Φ, and Φ^* with respect to the normalized depth z/H for different values of the irregularity-depth parameter h_0/a. The valid mathematical range of h/a can be written as $0 \leq h_0/a < 2$. The chosen values of h_0/a are 0.00, 0.04, and 0.08 for all the plots. The case $h_0/a = 0$ corresponds to a perfectly regular upper surface with no geometric disturbance.

Figure 3(a) shows that $\Upsilon_{zz}^{nl}H/L_0$ increases as h_0/a becomes larger. The curves shift upward with increasing irregularity depth, indicating that a deeper parabolic irregularity intensifies the

ARTICLE IN PRESS

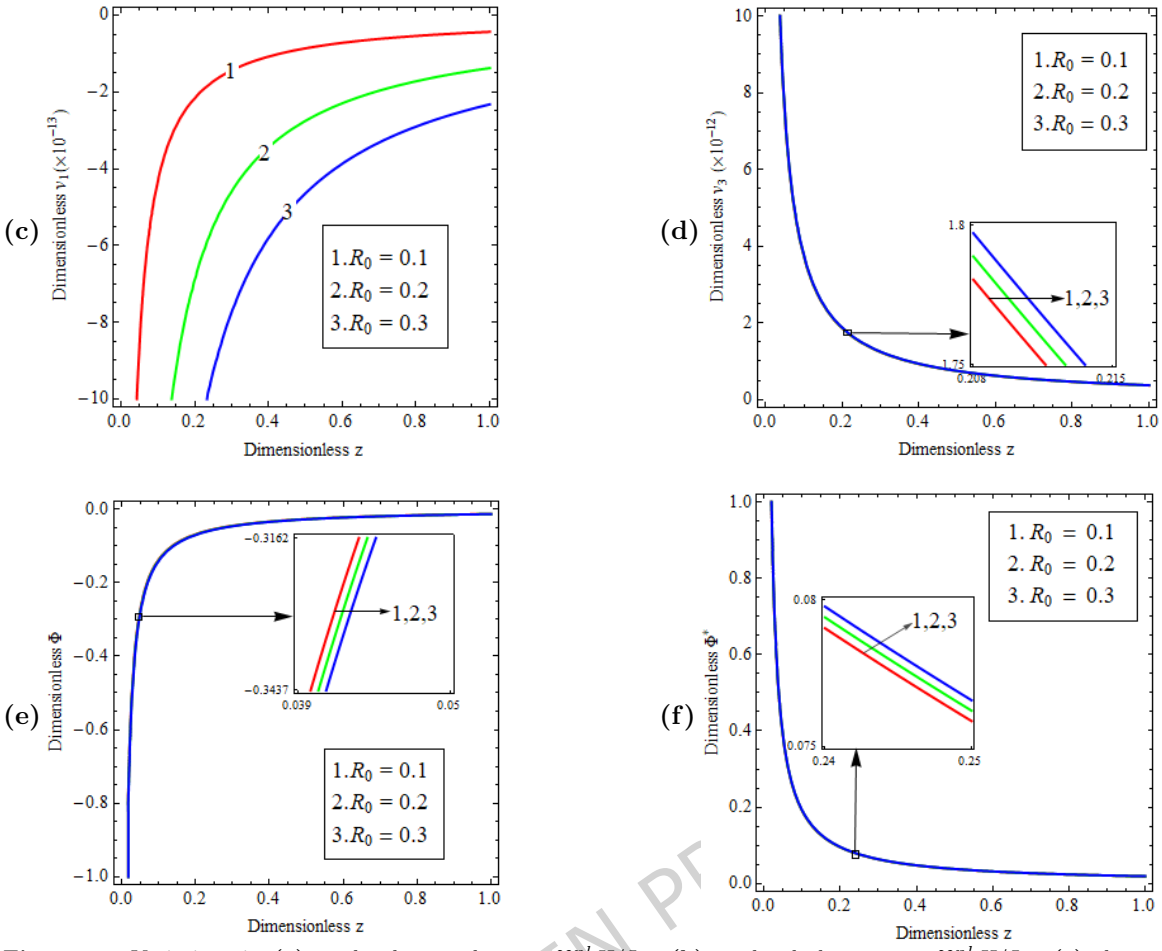


Figure 2. Variations in **(a)** nonlocal normal stress $\Upsilon_{zz}^{nl}H/L_0$, **(b)** nonlocal shear stress $\Upsilon_{zx}^{nl}H/L_0$, **(c)** the horizontal displacement component v_1, **(d)** the vertical displacement component v_3, **(e)** the electric potential of solid Φ, and **(f)** the electric potential of fluid phase Φ^* for different values of frictional coefficient $\mathcal{R}_0$.

normal stress throughout the layer. The maximum stress occurs near the upper boundary ($z \to 0$) and decreases rapidly with depth, approaching nearly zero around $z = 1$. A similar trend is observed for the shear stress in Figure 3(b), where the stress level rises with the increasing irregularity depth. The differences among successive curves in both Figures 3(a) and 3(b) are relatively small. In all cases, the stresses tend to vanish as z approaches unity.

The displacement behaviour presented in Figures 3(c) and 3(d) reveals that v_1 decreases with increasing h_0/a, while v_3 exhibits an opposite trend and increases as the irregularity depth grows. The influence of h_0/a on v_1 is minimal, whereas in the case of v_3 the curves remain close but show a consistent upward shift with increasing h_0/a.

Figure 3(e) demonstrates that the electric potential Φ diminishes as h_0/a increases across the entire depth. Conversely, Figure 3(f) shows that the fluid-phase potential Φ^* increases with increasing irregularity depth. In both figures, the separation between consecutive curves is modest, indicating that the effect of h_0/a on the potentials, although noticeable, is not substantial.

7.3 *Effect of irregularity factor*

The influence of the irregularity factor (x/a) on the quantities $\Upsilon_{zz}^{nl}H/L_0$, $\Upsilon_{zx}^{nl}H/L_0$, v_1, v_3, Φ, and Φ^* is presented in Figures 4(a)–4(f), respectively. The valid mathematical range of x/a is $[0, 1]$. In all cases, the initial value $x/a = 0$ corresponds to a rectangular irregularity on the rough upper surface. Thereafter, x/a is increased to 0.5 and 1.0 and the curve for $x/a = 1$ corresponds

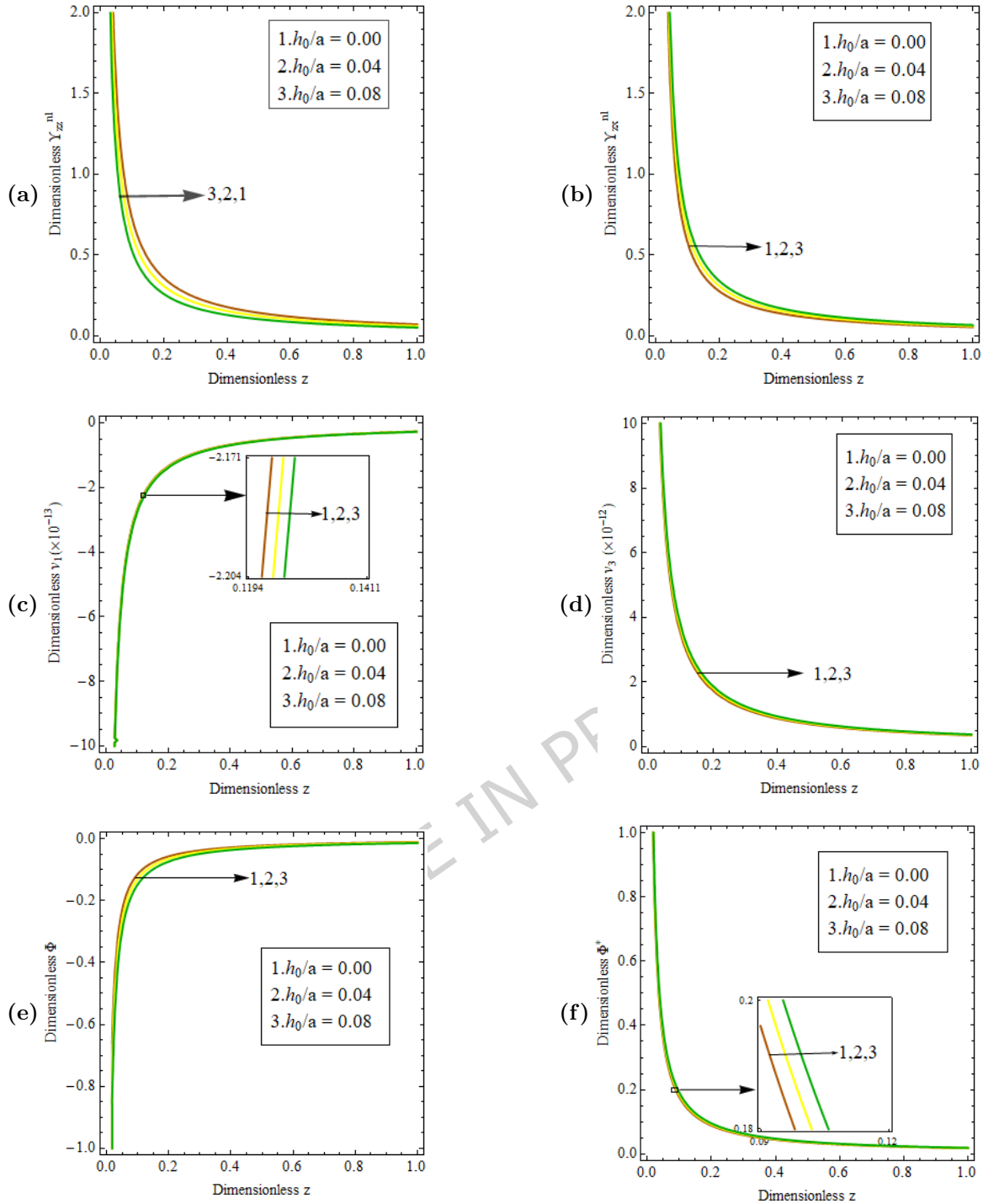


Figure 3. Variations in **(a)** nonlocal normal stress $\Upsilon_{zz}^{nl}H/L_0$, **(b)** nonlocal shear stress $\Upsilon_{zx}^{nl}H/L_0$, **(c)** the horizontal displacement component v_1, **(d)** the vertical displacement component v_3, **(e)** the electric potential of solid Φ, and **(f)** the electric potential of fluid phase Φ^* for different values of irregularity depth h_0/a.

to a configuration without irregularity.

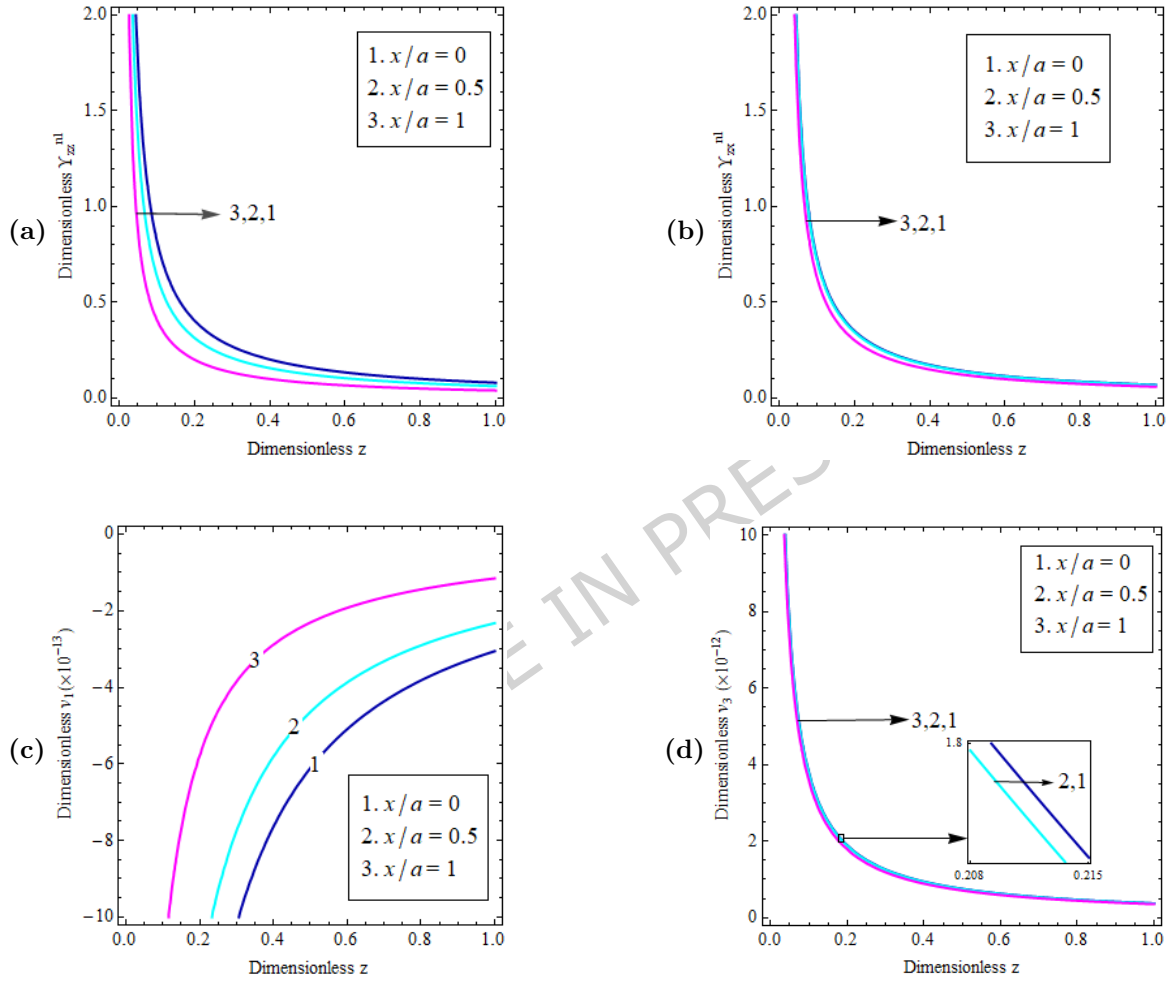
Figures 4(a) and 4(b) demonstrate that both $\Upsilon_{zz}^{nl}H/L_0$ and $\Upsilon_{zx}^{nl}H/L_0$ decrease as x/a increases. This inverse relationship suggests that as the irregularity transitions from a pronounced parabolic shape ($x/a = 0$) toward a flat surface ($x/a = 1$), the stresses reduce, potentially indicating enhanced stability or increased material resistance due to reduced geometric disturbance. The spacing between successive curves is more noticeable in Figure 4(a) compared to Figure 4(b).

The displacement response exhibits contrasting behavior. Figure 4(c) shows that v_1 increases

ARTICLE IN PRESS

with x/a, whereas Figure 4(d) reveals that v_3 decreases as x/a approaches unity. The effect of the irregularity factor on v_1 is clearly pronounced throughout the depth, while in the case of v_3 the curves remain close, indicating only minor variations. Thus, the parameter x/a has a stronger influence on the horizontal displacement v_1 than on the vertical displacement v_3.

The electric potential profiles in Figures 4(e) and 4(f) further complement these trends. As x/a increases, the solid-phase potential Φ shifts upward, showing an overall increase. In contrast, the fluid-phase potential Φ^* decreases for larger values of x/a. In both figures, the differences between the consecutive curves are modest, indicating that the impact of the irregularity factor on the potentials, although consistent, remains relatively small.



7.4 *Effect of nonlocality parameter*

Figures 5(a)–5(f) illustrate the influence of the nonlocal parameter ε_0 on the quantities $\Upsilon_{zz}^{nl}H/L_0$, $\Upsilon_{zx}^{nl}H/L_0$, v_1, v_3, Φ, and Φ^*, respectively. Curves 1, 2, and 3 correspond to $\varepsilon_0 = 0.00,\ 0.02$, and 0.04, where $\varepsilon_0(<<1) = 0$ denotes the purely local case with no nonlocal interactions.

Figures 5(a) and 5(b) reveal that increasing ε_0 leads to a increment in both $\Upsilon_{zz}^{nl}H/L_0$ and $\Upsilon_{zx}^{nl}H/L_0$, indicating a direct relationship between the stresses and the nonlocality parameter. In Figure 5(a), the curves remain close to each other for $z \in [0.2, 1]$, showing minimal sensitivity to ε_0 near the lower surface. For $z \in [0, 0.2]$, noticeable differences appear after which the curves converge and exhibit negligible variation as z approaches unity. A similar behaviour is observed in Figure 5(b). However, the impact of nonlocality paramter ε_0 is significant on shear stress compared to normal stress.

ARTICLE IN PRESS

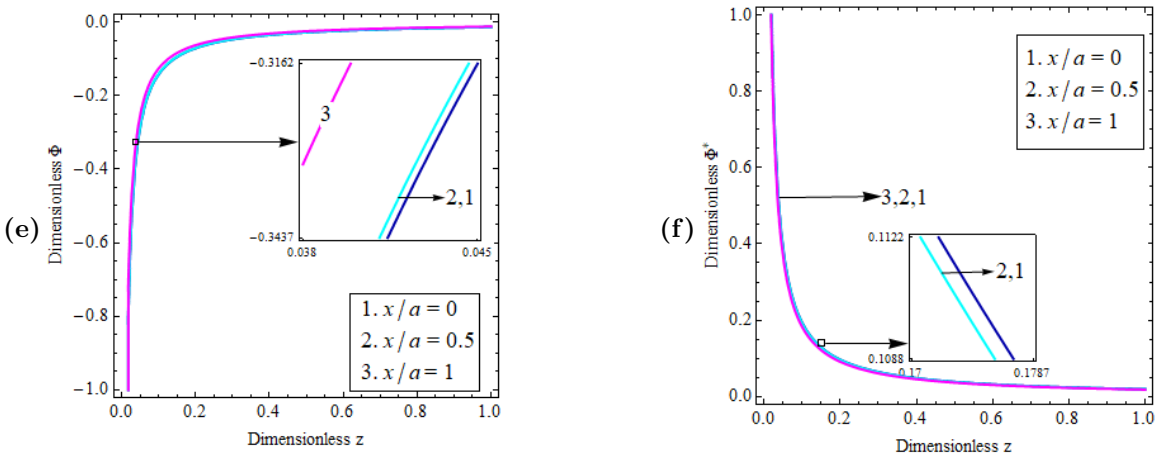
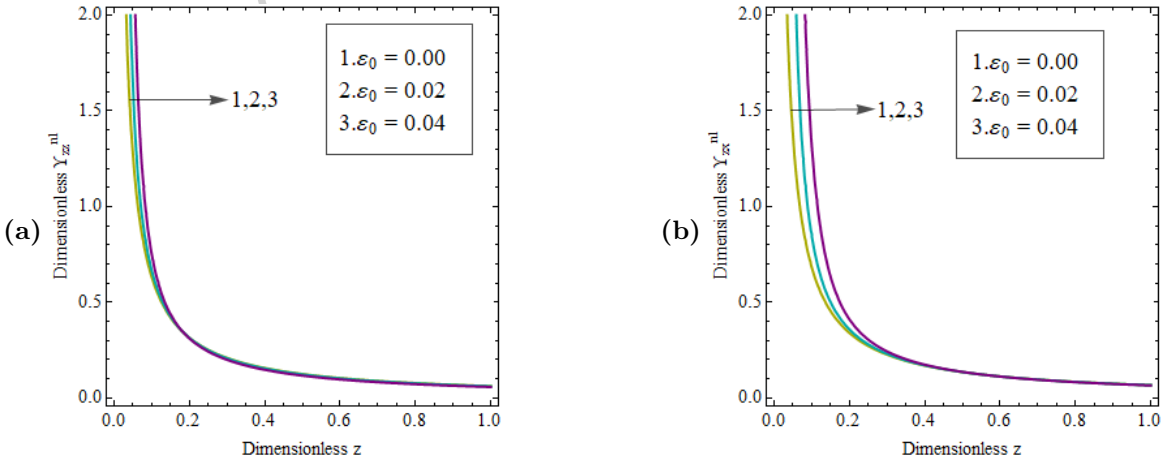


Figure 4. Variations in **(a)** nonlocal normal stress $\Upsilon_{zz}^{nl}H/L_0$, **(b)** nonlocal shear stress $\Upsilon_{zx}^{nl}H/L_0$, **(c)** the horizontal displacement component v_1, **(d)** the vertical displacement component v_3, **(e)** the electric potential of solid Φ, and **(f)** the electric potential of fluid phase Φ^* for different values of irregularity factor x/a.

The displacement components show similar trends. In figure 5(c), the negative sign on the vertical axis actually represents the direction of the displacement component (v_1) which eventually indicates that contraction is occurring in case of v_1. As ε_0 increases, the magnitude of v_1 increases but in the opposite direction. Therefore, it can be concluded that the horizontal displacement component is not decreasing with respect to the increase in ε_0, rather the magnitude shows ascending trend but it is increasing in the opposite direction of the positive x-axis. Therefore, both v_1 and v_3 exhibit same nature, i.e. ascending trend along with ε_0. The differences between successive curves in both figures are appreciable, with the change from Curve 2 to Curve 3 being more pronounced than the change from Curve 1 to Curve 2. This suggests that the influence of nonlocality becomes increasingly significant at higher values of ε_0.

The electric potential responses follow consistent patterns as observed for displacement components. In Figure 5(e), the magnitude of solid-phase potential Φ increases with increasing ε_0. However, the separation between the curves is extremely small, implying that nonlocality has only a minor effect on Φ. In contrast, Figure 5(f) shows a clear rise in the fluid-phase potential Φ^* with increasing ε_0, particularly over the initial portion of the depth. As z approaches unity, all curves in Figure 5(f) flatten out and tend toward zero.

ARTICLE IN PRESS



7.5 *Effect of Moving load velocity*

Figures 6(a)–6(f) illustrate the influence of the moving load velocity $\mathcal{V}_0$ on the quantities $\Upsilon_{zz}^{nl}H/L_0$, $\Upsilon_{zx}^{nl}H/L_0$, v_1, v_3, Φ, and Φ^*, respectively. Curves 1, 2, and 3 correspond to $\mathcal{V}_0 = 10,\ 12$, and 14,

ARTICLE IN PRESS

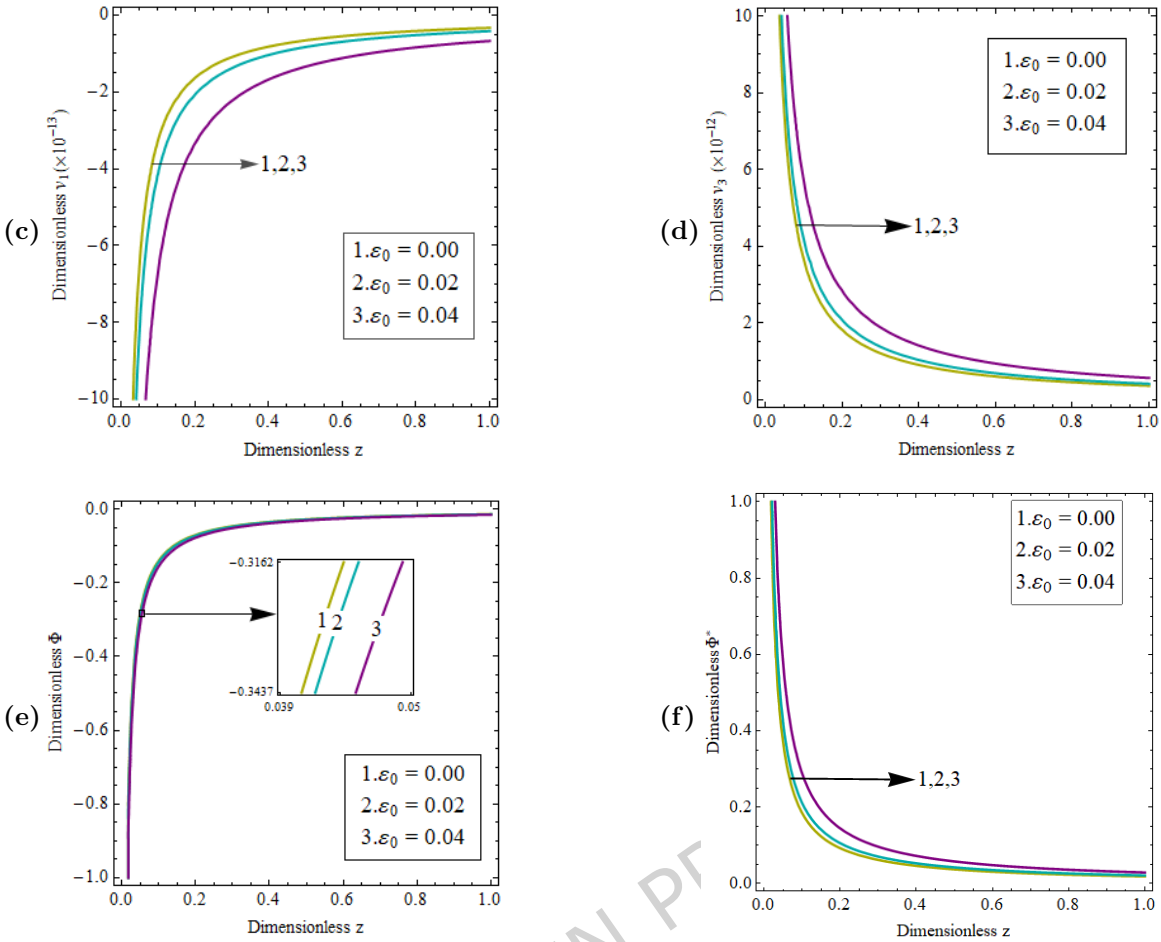


Figure 5. Variations in **(a)** nonlocal normal stress $\Upsilon_{zz}^{nl} H/L_0$, **(b)** nonlocal shear stress $\Upsilon_{zx}^{nl} H/L_0$, **(c)** the horizontal displacement component v_1, **(d)** the vertical displacement component v_3, **(e)** the electric potential of solid Φ, and **(f)** the electric potential of fluid phase Φ^* for different values of nonlocality parameter ε_0.

respectively. These graphical implementations are valid when $\mathcal{V}_0$ assumes any positive magnitude.

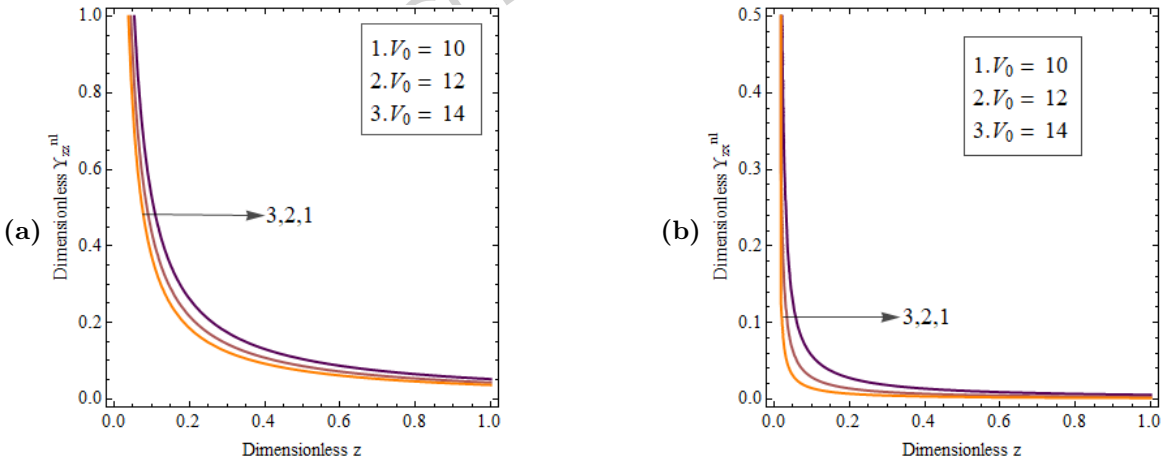
Figures 6(a) and 6(b) illustrate the influence of the moving load velocity $\mathcal{V}_0$ on the dimensionless nonlocal normal stress $\Upsilon_{zz}^{nl} H/L_0$ and nonlocal shear stress $\Upsilon_{zx}^{nl} H/L_0$, respectively. In both plots, curves 1, 2, and 3 correspond to velocities $\mathcal{V}_0 = 10, 12$, and 14, respectively. From Figure 6(a), it is observed that as the velocity $\mathcal{V}_0$ increases, the magnitude of the normal stress significantly diminishes. A similar trend is depicted in Figure 6(b) for the nonlocal shear stress, where higher load velocities lead to a clear reduction in the stress amplitudes across the spatial domain. This reveals a consistent inverse relationship between the moving load velocity and the dynamic stress components within the porous piezoelectric layer. The observed reduction in stress magnitudes with increasing velocity can be physically attributed to the dynamic lag and inertia effects inherent in the nonlocal porous piezoelectric medium. At higher velocities, the load traverses the surface faster than the characteristic time required for the piezoelectric skeleton to fully develop its electromechanical strain response. Consequently, the material does not reach its full static-equivalent deformation, preventing the accumulation of high localized stress concentrations. Furthermore, within Eringen's nonlocal framework, the internal characteristic length scale facilitates a spatial averaging of the external force. As the load speed increases, the energy is distributed more broadly across the nonlocal neighborhood rather than being focused at a single point, thereby lowering the stress intensity. This behavior suggests that the NPPEL structure exhibits a "velocity-induced shielding" effect, which is a critical consideration for the durability of micro-devices subjected to high-speed dynamic loading.

Figures 6(c) and 6(d) illustrate the variation of the horizontal displacement component (v_1) and

ARTICLE IN PRESS

the vertical displacement component (v_3) across the spatial domain for different values of moving load velocity ($\mathcal{V}_0$). Curves 1, 2, and 3 correspond to $\mathcal{V}_0 = 10, 12$, and 14, respectively. Observation of Figure 6(c) indicates that the horizontal displacement v_1 reaches its maximum magnitude near the point of load application and gradually attenuates. As the velocity $\mathcal{V}_0$ increases, there is a prominent reduction in the amplitude of v_1, moving from curve 1 to curve 3. Similarly, Figure 6(d) reveals that the vertical displacement v_3 follows a matching trend, where higher load velocities lead to a systematic decrease in the vertical deformation peaks. These results confirm that increasing the speed of the moving load exerts a dampening effect on the overall mechanical deformation of the nonlocal porous piezoelectric layer. The reduction in displacement components with increasing velocity is primarily attributed to the dynamic stiffening effect and the mechanical inertia of the porous piezoelectric aggregate. At lower velocities, the material has sufficient time to respond to the external excitation, allowing the strain field to develop fully. However, as the velocity $\mathcal{V}_0$ increases, the duration of the load's interaction with any specific localized region of the plate decreases.

Figures 6(e) and 6(f) illustrate the influence of the moving load velocity $\mathcal{V}_0$ on the electric potential of the solid phase (ϕ) and the fluid phase (ϕ^*), respectively. Curves 1, 2, and 3 correspond to velocities $\mathcal{V}_0 = 10, 12$, and 14. From Figure 6(e), it is observed that ϕ takes negative values, indicating a specific polarity in the induced electric field. As $\mathcal{V}_0$ increases, the curves move closer to the zero-axis, which signifies a decrease in the absolute magnitude $|\phi|$. Similarly, Figure 6(f) shows that the positive magnitude of the fluid-phase potential ϕ^* decreases consistently with the rising values of velocity. These results indicate that higher load speeds lead to a general reduction in the induced electrical response across both phases of the porous piezoelectric medium.Physical SignificanceThe reduction in the magnitude of ϕ and ϕ^* with increasing velocity is directly linked to the electromechanical coupling efficiency and the dynamic lag of the system. In a piezoelectric material, the electric potential is generated as a direct result of mechanical strain. As established in the displacement analysis (Figures 6c and 6d), higher load velocities result in smaller mechanical deformations because the material's inertia prevents it from responding fully to a fast-moving transient load.



7.6 *Comparative analysis for normal and shear stresses*

Figures 7(a) and 7(b) present a quantitative validation of the current model against the established work of Rakshit et al. [21]. In both figures, the solid lines represent the results of the present study, while the dashed lines represent the results of the comparative model under the limiting conditions of $\varepsilon_0 = 0$ (local limit) and $z \to \infty$ (half-space approximation). The graphical comparison reveals that the stress profiles in both studies follow an identical trend, exhibiting excellent qualitative agreement. This alignment confirms the accuracy of the mathematical formulation and numerical

ARTICLE IN PRESS

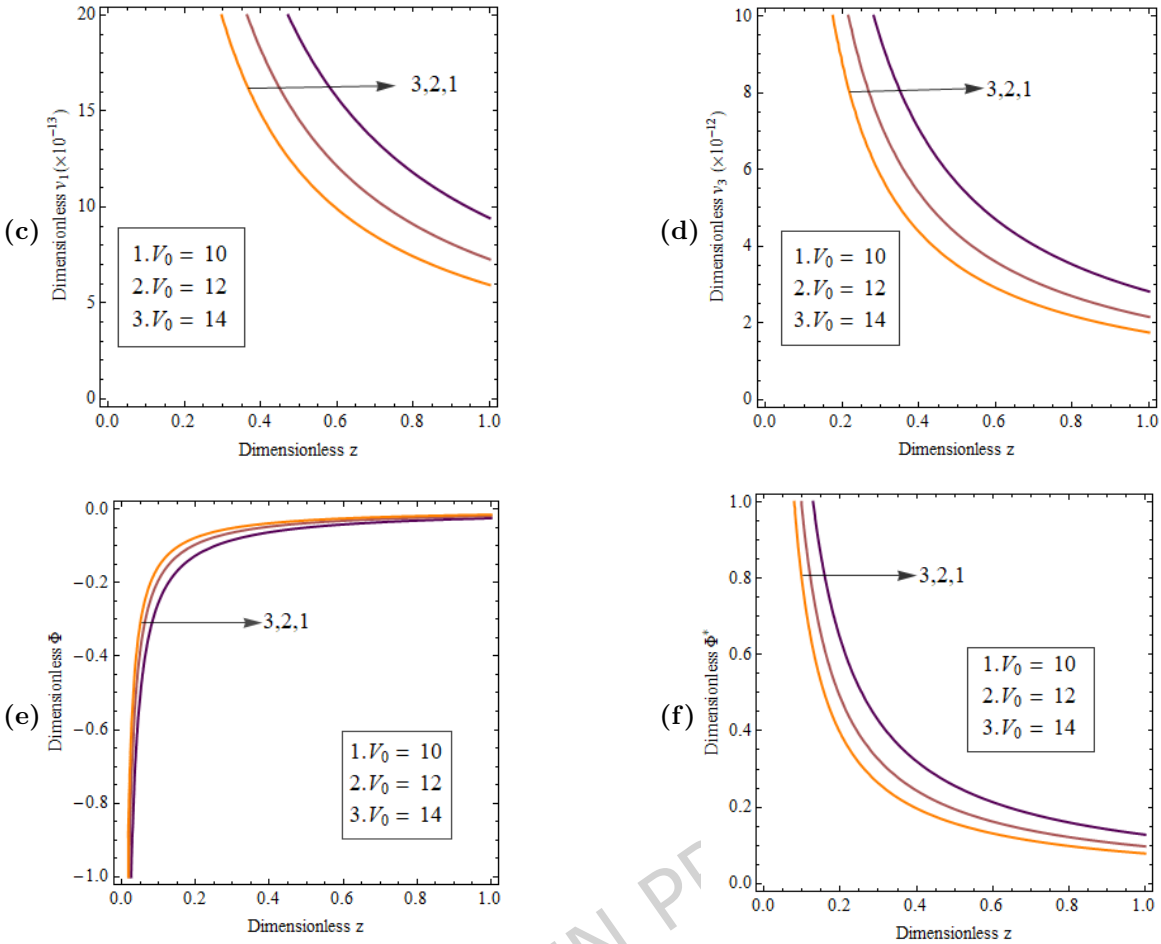


Figure 6. Variations in **(a)** nonlocal normal stress $\Upsilon_{zz}^{nl}H/L_0$, **(b)** nonlocal shear stress $\Upsilon_{zx}^{nl}H/L_0$, **(c)** the horizontal displacement component v_1, **(d)** the vertical displacement component v_3, **(e)** the electric potential of solid Φ, and **(f)** the electric potential of fluid phase Φ^* for different values of Velocity $\mathcal{V}_0$.

algorithm employed in the current analysis. However, a distinct quantitative difference is observed: the magnitudes of both the normal stress (Fig. 7a) and shear stress (Fig. 7b) in the present work are consistently higher than those reported by Rakshit et al. [21]. The enhancement in stress magnitudes in the present model is primarily attributed to the consideration of the nonlocal layered structure rather than a local half-space, leading to internal wave reflections and energy confinement that amplify the dynamic stress response compared to the semi-infinite medium used in the comparative model. Furthermore, the incorporation of nonlocal effects stiffens the material which results in the increasing nature of both normal and shear stresses in the present model. This validation proves that while our model recovers the classical trends, it provides a more realistic and conservative estimate of the stresses in irregular porous piezoelectric structures.

ARTICLE IN PRESS

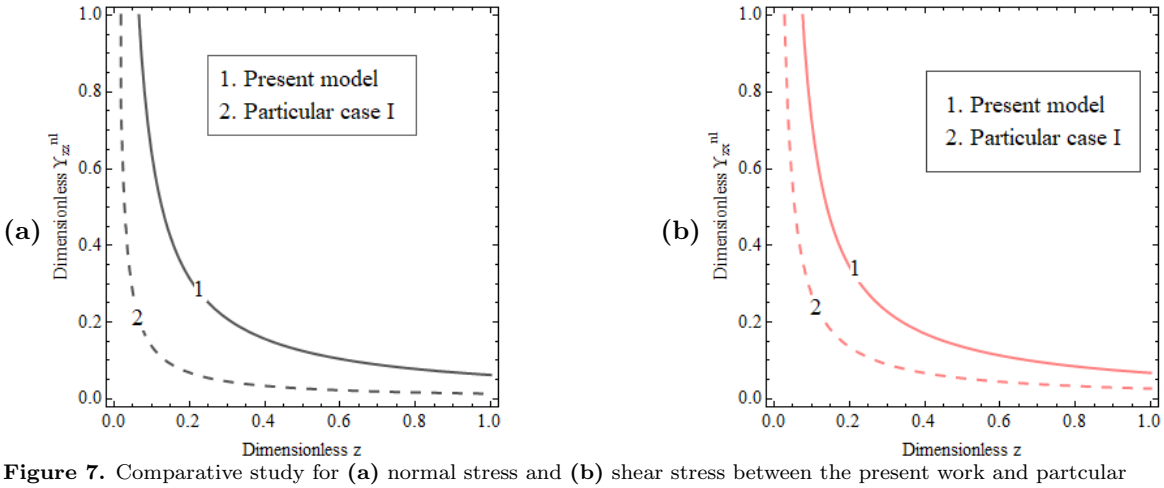


Figure 7. Comparative study for **(a)** normal stress and **(b)** shear stress between the present work and partcular case I (Rakshit et al. [21]).

8. Conclusions

The key conclusions of this investigation can be summarized as follows:

- The frictional coefficient $\mathcal{R}_0$ serves as a critical measure of the drag and resistance experienced by the plate as the load traverses its upper surface. Physically, a moving load generates both vertical pressure and a horizontal frictional force that opposes motion; $\mathcal{R}_0$ represents the shear coupling between this load and the plate, acting as the primary parameter controlling the magnitude of resulting stress fields and the susceptibility of the micro/nano device to fatigue or cracking. In the present model, this coefficient significantly amplifies the nonlocal normal stress Υ_{zz}^{nl} and alters both displacement components. However, while it acts as a crucial driver for normal stress and structural deformation, its influence on the nonlocal shear stress Υ_{zx}^{nl} and the resulting electric potentials remains comparatively weak.

- The irregularity depth ratio h_0/a is a dimensionless parameter that quantifies the severity of surface imperfections, representing the maximum indentation depth of the superficial parabolic discontinuity on the upper boundary of the micro/nano plate. An increase in h_0/a values leads to a decrease in the nonlocal normal stress Υ_{zz}^{nl}, while simultaneously causing an increase in the nonlocal shear stress near the upper rough surface. This indicates that while the deepening of the irregularity may mitigate normal stress, it intensifies shear-related stress concentrations at the interface, serving as a critical factor in the potential failure of the plate. Despite these significant impacts on nonlocal stresses, the influence of the irregularity depth on displacement components and electric potentials remains minimal throughout the depth of the structure.

- The irregularity span ratio x/a serves as a critical geometric parameter, with numerical results demonstrating that all mechanical and electrical variables decrease as the irregularity span value increases. Physically, this ratio normalizes the horizontal coordinate x—which coincides with the direction of the applied load—against a, half the total span of the parabolic defect $(2a)$. The study of x/a reveals that the maximum stress concentration and peak displacements occur at the center of the parabolic irregularity $(x/a = 0)$, followed by a consistent decline as one moves toward the flat edges of the plate. While this factor strongly governs the in-plane displacement v_1 and significantly modifies the nonlocal normal stress Υ_{zz}^{nl}, it exerts a minimal impact on the nonlocal shear stress Υ_{zx}^{nl}, the vertical displacement v_3, and the electric potentials for both the solid and fluid phases. This suggests that while the severity of the surface defect dictates the primary load-bearing response, its influence on shear and potential distributions is relatively secondary.

ARTICLE IN PRESS

- The nonlocality parameter ε_0 is utilized to capture small-scale effects in micro- and nano-scale structures that are otherwise neglected by classical continuum mechanics. Increasing this parameter results in a simultaneous ascent of all physical variables, characterized by an enhancement in both nonlocal stress profiles and displacement fields (v_1 and v_3). This uniform increment across all variables indicates a significant nonlocal stiffening effect that reinforces the overall structural response. Physically, this behavior demonstrates that a higher ε_0 leads to elevated peak values for normal and shear stresses, which serves to improve the material's resistance against localized failure and crack propagation.

- As a moving load travels faster across a surface, the intensity of its impact—including stress, physical movement (displacements), and electric potentials—actually decreases. This happens because at high speeds, the load passes over a specific point so quickly that the material doesn't have enough time to fully react or sink. Physically, this can be understood through the concept of material "stiffness" under fast loading: the material behaves more rigidly because the atoms and fibers cannot move out of the way fast enough.

- For all parameters considered, the strongest variations occur near the upper irregular surface, with stresses and displacements decaying rapidly and approaching zero as $z \to 1$, confirming the physical consistency of the model.

9. Applications

The results obtained from the present model can be applicable in following areas:

- The model helps predict the fatigue life and failure points of piezoelectric diaphragm sensors. Manufacturing processes often leave surface imperfections (like the parabolic irregularity studied). The model can determine the critical tolerance for these surface defects before a moving load (e.g., fluid flow, shock wave) causes stress concentrations that lead to device failure. It is used to design and analyze Surface Acoustic Wave (SAW) or Bulk Acoustic Wave (BAW) devices where the propagation of mechanical waves is influenced by the device's porous structure and surface finish.

- Piezoelectric plates are used as mechanical filters. The thickness, porosity, and boundary conditions (including surface defects) directly affect the device's resonant frequency. The model's ability to accurately predict dynamic stress fields allows engineers to tune the structural response and filter characteristics precisely. It provides insight into how the nonlocal effects and porosity affect the material's ability to damp out vibrations or absorb mechanical shocks from a moving source.

- Beyond its theoretical framework, this study provides actionable design metrics for the fabrication and quality control of micro-electromechanical systems (MEMS). Specifically, the quantitative analysis of stress concentration as a function of the parabolic irregularity depth (h_0/s) allows for the establishment of precise manufacturing tolerance limits. For instance, the results indicate that while normal stress exhibits a stress-relief trend, the shear stress concentration increases significantly as the irregularity depth ratio exceeds 0.1. In a MEMS fabrication context—such as the chemical etching of PZT-5H micro-plates—a process engineer can utilize these curves to set a "Critical Defect Threshold". By mapping the peak shear stress values against the material's mechanical yield strength and depolarization limits, a maximum allowable surface roughness of $h_0/s \leq 0.1$ can be established to prevent premature fatigue failure or signal degradation under frictional moving loads. This transforms the observed stress-field sensitivities into a rigorous "Design-for-Reliability" (DfR) protocol, enabling a strategic balance between high-precision manufacturing costs and the operational longevity of smart micro-devices.

ARTICLE IN PRESS

Acknowledgements

This article has been produced with the financial support of the European Union under the REFRESH – Research Excellence For Region Sustainability and High-tech Industries project number CZ.10.03.01/00/22_003/0000048 via the Operational Programme Just Transition.

Funding

This article has been produced with the financial support of the European Union under the RE-FRESH - Research Excellence For Region Sustainability and High-tech Industries project number CZ.10.03.01/00/22_003/0000048 via the Operational Programme Just Transition.

Authorship statement

Meghana A R: Supervision, Methodology. **Soumik Das:** Validation, Writing- Reviewing and Editing. **Rachaita Dutta:** Investigation, Writing- Original draft preparation. **Vipin Gupta:** Conceptualization. **Murat Yaylacı**: Software. **Faisal Muteb K. Almalki:** Methodology. **Mohammad Ghatasheh:** Visualization. **Aymen Flah:** Software, Writing- Reviewing and Editing, Validation.

Declaration of competing interests

The authors have no competing interests to declare.

Declaration of generative AI use

This statement confirms that the authors did not use AI in the core process

Data availability

All data generated or analysed during this study are included in this published article.

ARTICLE IN PRESS

Appendix

$$m_1=\left(\mathcal{C}_{11}-\frac{(\varrho_{12})_{11}}{(\varrho_{22})_{11}}\mathcal{M}_{11}\right),m_2=\left(\mathcal{C}_{44}+\mathcal{C}_{13}-\frac{(\varrho_{12})_{11}}{(\varrho_{22})_{11}}\mathcal{M}_{33}\right),m_3=\left(\mathcal{E}_{31}+\mathcal{E}_{15}-\chi_3^*\frac{(\varrho_{12})_{11}}{(\varrho_{22})_{11}}\right),$$
$$m_4=\left(\chi_{31}+\chi_{15}-\mathcal{E}_3^*\frac{(\varrho_{12})_{11}}{(\varrho_{22})_{11}}\right),m_5=\left(\mathcal{C}_{44}+\mathcal{C}_{13}-\frac{(\varrho_{12})_{33}}{(\varrho_{22})_{33}}\mathcal{M}_{11}\right),m_6=\left(\mathcal{C}_{33}-\frac{(\varrho_{12})_{33}}{(\varrho_{22})_{33}}\mathcal{M}_{33}\right),$$
$$m_7=\left(\mathcal{E}_{33}-\chi_3^*\frac{(\varrho_{12})_{33}}{(\varrho_{22})_{33}}\right),m_8=\left(\chi_{33}-\frac{(\varrho_{12})_{33}}{(\varrho_{22})_{33}}\mathcal{E}_3^*\right),m_9=\mathcal{E}_{15}+\mathcal{E}_{31},m_{10}=\chi_{31}+\chi_{15},$$
$$n_1=\mathcal{C}_{44}-d'_{11}\varepsilon_0k^2\mathcal{V}_0^2,n_2=-\mathcal{M}_{11}+d'_{11}\varepsilon_0k^2\mathcal{V}_0^2+d'_{11}\mathcal{V}_0^2,$$
$$n_3=-\mathcal{C}_{44}+d'_{33}\varepsilon_0k^2\mathcal{V}_0^2+d'_{33}\mathcal{V}_0^2,n_4=m_6-d'_{33}\varepsilon_0k^2\mathcal{V}_0^2.$$
$$p_i=\mathcal{C}_{33}\Theta_i^{(1)}+\mathcal{E}_{33}\Theta_i^{(2)}+\chi_{33}\Theta_i^{(3)},s_i=\mathcal{C}_{44}\Theta_i^{(1)}+\mathcal{E}_{15}\Theta_i^{(2)}+\chi_{15}\Theta_i^{(3)},$$
$$t_i=\mathcal{C}_{33}\Psi_i^{(1)}+\mathcal{E}_{33}\Psi_i^{(2)}+\chi_{33}\Psi_i^{(3)},r_i=\mathcal{C}_{44}\Psi_i^{(1)}+\mathcal{E}_{15}\Psi_i^{(2)}+\chi_{15}\Psi_i^{(3)},$$
$$w_i=\mathcal{C}_{13}\Theta_i^{(1)}+\mathcal{E}_{31}\Theta_i^{(2)}+\chi_{31}\Theta_i^{(3)},y_i=\mathcal{C}_{13}\Psi_i^{(1)}+\mathcal{E}_{31}\Psi_i^{(2)}+\chi_{31}\Psi_i^{(3)},\text{ for } i=1,2,3,4.$$

References

[1] Bahl S, Nagar H, Singh I, et al. Smart materials types, properties and applications: A review. Materials Today: Proceedings. 2020;28:1302–1306.

ARTICLE IN PRESS

[2] Uchino K. Piezoelectric actuators and ultrasonic motors. Vol. 1. Springer Science & Business Media; 1996.

[3] Kar-Gupta R, Venkatesh T. Electromechanical response of porous piezoelectric materials. Acta Materialia. 2006;54(15):4063–4078.

[4] Wang F, Han X, Ding T. An anisotropic layered poroelastic half-space subjected to a moving point load. Soil Dynamics and Earthquake Engineering. 2021;140:106427.

[5] Muho EV. Dynamic response of an elastic plate on a transversely isotropic viscoelastic half-space with variable with depth moduli to a rectangular moving load. Soil Dynamics and Earthquake Engineering. 2020;139:106330.

[6] Mallik AK, Chandra S, Singh AB. Steady-state response of an elastically supported infinite beam to a moving load. Journal of sound and vibration. 2006;291(3-5):1148–1169.

[7] Frỳba L. Vibration of solids and structures under moving loads. Vol. 1. Springer science & business media; 2013.

[8] Shamalta M, Metrikine A. Analytical study of the dynamic response of an embedded railway track to a moving load. Archive of Applied Mechanics. 2003;73(1):131–146.

[9] Frỳba L. Dynamic interaction of vehicles with tracks and roads. Vehicle System Dynamics. 1987;16(3):129–138.

[10] Yang YB, Yau J, Yao Z, et al. Vehicle-bridge interaction dynamics: with applications to high-speed railways. World Scientific; 2004.

[11] Sneddon IN. The stress produced by a pulse of pressure moving along the surface of a semi-infinite solid. Rendiconti del Circolo Matematico di Palermo. 1952;1(1):57–62.

[12] Ang DD. Transient motion of a line load on the surface of an elastic half-space. Quarterly of Applied Mathematics. 1960;18(3):251–256.

[13] Payton RG. Transient motion of an elastic half-space due to a moving surface line load. International Journal of Engineering Science. 1967;5(1):49–79.

[14] Sackman J. Uniformly moving load on a layered half plane. Journal of the Engineering Mechanics Division. 1961;87(4):75–89.

[15] Chatterjee M, Chattopadhyay A. Effect of moving load due to irregularity in ice sheet floating on water. Acta Mechanica. 2017;228(5):1749–1765.

[16] Kumar P, Chattopadhyay A, Mahanty M, et al. Stresses induced by a moving load in a composite structure with an incompressible poroviscoelastic layer. Journal of Engineering Mechanics. 2019;145(9):04019062.

[17] Kaur T, Sharma SK, Singh AK. Dynamic response of a moving load on a micropolar half-space with irregularity. Applied Mathematical Modelling. 2016;40(5-6):3535–3549.

[18] Malekzadeh P, Monajjemzadeh S. Nonlinear response of functionally graded plates under moving load. Thin-Walled Structures. 2015;96:120–129.

[19] Rybyanets AN. Porous piezoceramics: theory, technology, and properties. IEEE transactions on ultrasonics, ferroelectrics, and frequency control. 2011;58(7):1492–1507.

[20] Chen S, Zhang Q, Liu H. Dynamic response of double-FG porous beam system subjected to moving load. Engineering with Computers. 2022;38(Suppl 3):2309–2328.

ARTICLE IN PRESS

ARTICLE IN PRESS

[21] Rakshit S, Mistri KC, Das A, et al. Stress analysis on the irregular surface of visco-porous piezoelectric half-space subjected to a moving load. Journal of Intelligent Material Systems and Structures. 2022;33(10):1244–1270.

[22] Yang J. An introduction to the theory of piezoelectricity. Springer; 2005.

[23] Balageas D, Fritzen CP, Güemes A. Structural health monitoring. Vol. 90. John Wiley & Sons; 2010.

[24] Galassi C. Processing of porous ceramics: Piezoelectric materials. Journal of the European Ceramic Society. 2006;26(14):2951–2958.

[25] Honein B, Braga A, Barbone P, et al. Wave propagation in piezoelectric layered media with some applications. Journal of intelligent material systems and structures. 1991;2(4):542–557.

[26] Bae DY, Lee JR. Development of single channeled serial-connected piezoelectric sensor array and damage visualization based on multi-source wave propagation imaging. Journal of Intelligent Material Systems and Structures. 2016;27(13):1861–1870.

[27] Gupta V, Kumawat S, Vishwakarma SK, et al. Effects of layer imperfections and material gradation on circumferential shear horizontal waves in cylindrical piezoelectric composite structure. Composite Structures. 2025;359:118997.

[28] Seema, Saeed AM, Singhal A, et al. Surface acoustic waves in a layered piezoelectric plate with considered surface effects. International Journal of Dynamics and Control. 2025;13(1):38.

[29] Cui J, Du J, Wang J. Effects of viscous liquid on sh wave propagation in layered viscoelastic/piezoelectric structure. In: 2014 IEEE International Ultrasonics Symposium; IEEE; 2014. p. 1971–1974.

[30] Liu H, Wang Z, Wang T. Effect of initial stress on the propagation behavior of love waves in a layered piezoelectric structure. International Journal of Solids and Structures. 2001; 38(1):37–51.

[31] Kumhar R, Kundu S, Maity M, et al. Analysis of interfacial imperfections and electromechanical properties on elastic waves in porous piezo-composite bars. International Journal of Mechanical Sciences. 2020;187:105926.

[32] Moharana S. Investigation of a continuum shear lag model as an indicator for the damage detection in piezo-elasto dynamic structure. Journal of Vibration Engineering & Technologies. 2021;9(7):1755–1768.

[33] Singh S, Barde A, Mahanty B, et al. Emerging technologies-based and digital twin driven inclusive manufacturing system. International Journal of Integrated Supply Management. 2020;13(4):353–375.

[34] Zhou Y, Lü C, Chen W. Bulk wave propagation in layered piezomagnetic/piezoelectric plates with initial stresses or interface imperfections. Composite Structures. 2012;94(9):2736–2745.

[35] Huang Y, Li XF. Interfacial waves in dissimilar piezoelectric cubic crystals with an imperfect bonding. IEEE transactions on ultrasonics, ferroelectrics, and frequency control. 2011; 58(6):1261–1265.

[36] Li P, Jin F. Excitation and propagation of shear horizontal waves in a piezoelectric layer imperfectly bonded to a metal or elastic substrate. Acta Mechanica. 2015;226(2):267–284.

[37] Eringen AC, Edelen D. On nonlocal elasticity. International journal of engineering science. 1972;10(3):233–248.

ARTICLE IN PRESS

ARTICLE IN PRESS

[38] Eringen AC. Theory of nonlocal thermoelasticity. International Journal of Engineering Science. 1974;12(12):1063–1077.

[39] Asghar S, Naeem MN, Hussain M, et al. Prediction and assessment of nonlocal natural frequencies of dwcnts: Vibration analysis. Computers and Concrete, An International Journal. 2020;25(2):133–144.

[40] Hussain M, Naeem MN, Tounsi A, et al. Nonlocal effect on the vibration of armchair and zigzag swcnts with bending rigidity. Advances in nano research. 2019;7(6):431–442.

[41] Zenkour AM, Abouelregal AE. Decaying temperature and dynamic response of a thermoelastic nanobeam to a moving load. Advances in computational design. 2018;3(1):1–16.

[42] Matouk H, Bousahla AA, Heireche H, et al. Investigation on hygro-thermal vibration of P-FG and symmetric S-FG nanobeam using integral timoshenko beam theory. Advances in nano research. 2020;8(4):293–305.

[43] Barati MR, Faleh NM, Zenkour AM. Dynamic response of nanobeams subjected to moving nanoparticles and hygro-thermal environments based on nonlocal strain gradient theory. Mechanics of Advanced Materials and Structures. 2019;26(19):1661–1669.

[44] Boutaleb S, Benrahou KH, Bakora A, et al. Dynamic analysis of nanosize FG rectangular plates based on simple nonlocal quasi 3d hsdt. Advances in nano research. 2019;7(3):191.

[45] Gupta S, Das S, Dutta R. Nonlocal stress analysis of an irregular FGFPM structure imperfectly bonded to fiber-reinforced substrate subjected to moving load. Soil Dynamics and Earthquake Engineering. 2021;147:106744.

[46] Dutta R, Das S, Bhengra N, et al. Nonlocal effect on shear wave propagation in a fiber-reinforced poroelastic layered structure subjected to interfacial impulsive disturbance. Soil Dynamics and Earthquake Engineering. 2024;176:108307.

[47] AR M, Dutta R, Gupta V, et al. Size-dependent analysis of surface wave in irregular fractured porous seabed subjected to fractional-order derivative. Mechanics of Advanced Materials and Structures. 2024;:1–22.

[48] Wang, Liyuan, Nan Chong, et al. Nonlinear vibration analysis of nonlocal fractional viscoelastic piezoelectric nanobeams incorporating surface effects. European Journal of Mechanics-A/Solids (2025);:105840.

[49] Mektout, Mohamed, and Hicham Bourouina. Nonlocal dynamic response of FGP sandwich microbeam with 2D PSH network incorporating adatoms-surface interactions energy under magnetic field. Mechanics of Advanced Materials and Structures, no. 15 (2025): 3632-3663.

[50] Mektout, Mohamed, Hicham Bourouina, et al. Functional resonator-based nonlocal FGP hollow adsorber for wide detection of coupled biomolecules using DQM framework. Meccanica (2025): 1-35.

[51] Mektout, Mohamed, Hicham Bourouina, Yahia Maiza, Soumia Khouni, and Abir Lamari. Size-dependent nonlocal resonance of smart phononic adsorber for biosensing under interatomic energy and magnetic intensity. Multiscale and Multidisciplinary Modeling, Experiments and Design , no. 1 (2026): 33.

[52] MAIZA, Yahia, Hicham Bourouina, Mohamed Mektout, et al. Nonlocal strain gradient-based nonlinear thermal effect on perforated FGP bio-resonator using DQM approach. Journal of Physics D: Applied Physics (2025).

ARTICLE IN PRESS

ARTICLE IN PRESS

[53] Maiza, Yahia, and Hicham Bourouina. Non-local response prediction for FGP sandwich microbeam with 2D PSH network subjected to adatoms-substrate interactions and exited by magnetic intensity. Acta Mechanica 236, no. 1 (2025): 259-288.

[54] Mektout, Mohamed, Hicham Bourouina, et al. Size-dependent nonlocal resonance of smart phononic adsorber for biosensing under interatomic energy and magnetic intensity. Multiscale and Multidisciplinary Modeling, Experiments and Design 9, no. 1 (2026): 33.

[55] Mektout, Mohamed, et al. Functional resonator-based nonlocal FGP hollow adsorber for wide detection of coupled biomolecules using DQM framework. Meccanica (2025): 1-35.

[56] Eringen AC, Wegner J. Nonlocal continuum field theories. Appl Mech Rev. 2003;56(2):B20–B22.

[57] Eringen AC. Plane waves in nonlocal micropolar elasticity. International Journal of Engineering Science. 1984;22(8-10):1113–1121.

[58] Gupta, Vishakha, and Anil K. Vashishth. The effects of piezoelectricity on the interaction of waves in fluid-loaded poroelastic half-space. Smart Materials Research 2014, no. 1 (2014): 281013.

[59] Kumari P, Modi C, Sharma V. Dynamic response of normal moving load on a transversely isotropic piezoelectric half-space with parabolic irregularity. Waves in Random and Complex Media. 2018;28(4):601–623.

[60] Chattopadhyay A, Gupta S, Sharma V, et al. Stresses produced on a rough irregular half-space by a moving load. Acta mechanica. 2011;221(3):271–280.

[61] Vashishth AK, Gupta V. Ultrasonic wave's interaction at fluid-porous piezoelectric layered interface. Ultrasonics. 2013;53(2):479–494.

[62] Li J, Dunn ML. Viscoelectroelastic behavior of heterogeneous piezoelectric solids. Journal of Applied Physics. 2001;89(5):2893–2903.

ARTICLE IN PRESS